

# triSurfaceImmersion: Computing volume fractions and signed distances from triangulated surfaces immersed in unstructured meshes

Tobias Tolle, Dirk Gründing, Dieter Bothe, Tomislav Marić\*

*Mathematical Modeling and Analysis Institute, Mathematics department, TU Darmstadt,  
Alarich-Weiss-Straße 10, 64287 Darmstadt, Germany*

---

## Abstract

We propose a numerical method that enables the calculation of volume fractions from triangulated surfaces immersed in unstructured meshes. First, the signed distances are calculated geometrically near the triangulated surface. For this purpose, the computational complexity has been reduced by using an octree space subdivision. Second, an approximate solution of the Laplace equation is used to propagate the inside/outside information from the surface into the solution domain. Finally, volume fractions are computed from the signed distances in the vicinity of the surface. The volume fraction calculation utilizes either geometrical intersections or a polynomial approximation based on signed distances. An adaptive tetrahedral decomposition of polyhedral cells ensures a high absolute accuracy. The proposed method extends the admissible shape of the fluid interface (surface) to triangulated surfaces that can be open or closed, disjoint, and model objects of technical geometrical complexity.

Current results demonstrate the effectiveness of the proposed algorithm for two-phase flow simulations of wetting phenomena, but the algorithm has broad applicability. For example, the calculation of volume fractions is crucial for achieving numerically stable simulations of surface tension-driven two-phase flows with the unstructured Volume-of-Fluid method. The method is applicable as a discrete phase-indicator model for the unstructured hybrid Level Set / Front Tracking method.

The implementation is available on GitLab [27].

This is a pre-print of the accepted article <https://doi.org/10.1016/j.cpc.2021.108249>, when citing, please refer to the accepted article.

### *Keywords:*

volume of fluid, triangular surface mesh, signed distances, unstructured mesh

---

## PROGRAM SUMMARY

*Program Title:* argo/triSurfaceImmersion

*CPC Library link to program files:* (to be added by Technical Editor)

*Developer's repository link:* <https://gitlab.com/leia-methods/argo>

---

\*Corresponding author

*Email addresses:* [tolle@mma.tu-darmstadt.de](mailto:tolle@mma.tu-darmstadt.de) (Tobias Tolle), [gruending@mma.tu-darmstadt.de](mailto:gruending@mma.tu-darmstadt.de) (Dirk Gründing), [bothe@mma.tu-darmstadt.de](mailto:bothe@mma.tu-darmstadt.de) (Dieter Bothe), [mari@mma.tu-darmstadt.de](mailto:mari@mma.tu-darmstadt.de) (Tomislav Marić)

*Code Ocean capsule:* (to be added by Technical Editor)

*Licensing provisions:* GPLv3

*Programming language:* C++

*Nature of problem:*

Computing volume fractions and signed distances from triangulated surfaces immersed in unstructured meshes.

*Solution method:*

First, the algorithm computes minimal signed distances between mesh points (cell centers and cell corner-points) and the triangulated surface, in the close vicinity of the surface. The sign is computed with respect to the surface normal orientation. Afterwards, the sign is propagated throughout the unstructured volume mesh by an approximate solution of a diffusion equation. The bulk cells' volume fractions are set, and interface cells are identified based on the signed distances. Volume fractions in cells intersected by the triangulated surface mesh are either computed by geometric intersections between surface triangles and a cell or by an approximation of the volume fraction approximation from signed distances, coupled with tetrahedral cell decomposition and refinement.

*Additional comments including restrictions and unusual features:*

The volume mesh can consist of cells of arbitrary shape. The surface mesh normal vectors need to be oriented consistently.

## 1. Introduction

We present a new numerical algorithm that calculates initial conditions for simulations of two-phase flow problems for fluid interfaces of complex shapes. The initial conditions are calculated in the form of signed distances and volume fractions from fluid interfaces approximated as arbitrarily shaped triangular surfaces immersed into unstructured meshes. The signed distances are relevant as initial conditions for the Level Set method [48, 49] for multiphase flow simulation. Volume fractions on unstructured meshes are required for the unstructured Volume-of-Fluid (VOF) method (cf. [30] for a recent review). In fact, we have applied the proposed algorithms to model experimental fluid interfaces from wetting experiments [16], which was not possible using available contemporary approaches that model fluid interfaces using (compositions of) implicit functions or parameterized surfaces. The proposed algorithm approximates the surfaces using triangle meshes that are omnipresent in Computer-Aided Design (CAD) because of their versatility: they can approximate basic surfaces such as spheres and ellipsoids, but also surfaces of mechanical parts, disjoint surfaces in mechanical assemblies, or surfaces resulting from imaging scans.

The overall simulation domain  $\Omega \subset \mathbb{R}^3$  is separated into two subdomains  $\Omega = \Omega^+(t) \cup \Omega^-(t)$ , representing phase 1 and phase 2, respectively, as illustrated for a liquid drop on a surface in fig. 1. At the contact line  $\Gamma := \partial\Omega \cap \overline{\Omega^+} \cap \overline{\Omega^-}$ , the liquid-gas interface  $\Sigma$  encloses a contact angle  $\theta$  with the solid surface  $\partial\Omega_{\text{wall}}$ . Furthermore, the normal vector  $\mathbf{n}_\Sigma$  of the interface  $\Sigma$  is oriented such that it points into the gas phase. Typically, a continuum mechanical model is used for the description of such fluid mechanical problems. This description is often based on a sharp interface model, as depicted in fig. 1. With this model, the liquid-gas interface can be described using an indicator function

$$\chi(\mathbf{x}, t) := \begin{cases} 1, & \mathbf{x} \in \Omega^- \subset \mathbb{R}^3 \\ 0, & \text{otherwise.} \end{cases} \quad (1)$$

An approximate solution of this model requires a decomposition of the solution domain into volumes

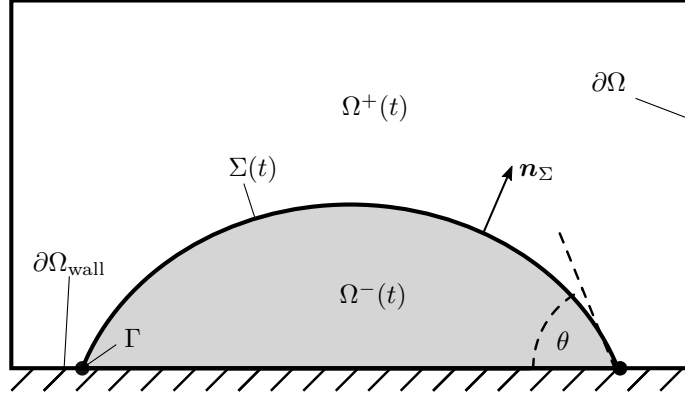


Figure 1: The different domains for a liquid (-) drop on a solid surface surrounded by a gas (+) phase.

that have no volume overlaps, the closed *cells*  $\Omega_c$ , denoted by

$$\Omega \approx \tilde{\Omega} = \{\Omega_c\}_{c \in C} \quad (2)$$

where  $C = \{1, 2, 3, \dots, N_c\}$  is a set of indices to mesh cells. As can be seen in fig. 2, the mesh is a set of non-overlapping subsets (*cells*)  $\Omega_c \subset \tilde{\Omega}$ . With non-overlapping, we mean that the volume of an intersection between any two cells is zero. *Index sets* represent the unstructured mesh data [15]. We consider a set of cell corner-points  $P_h$  where each point in  $P_h$  is an element of  $\mathbb{R}^3$ . Geometrically, each cell  $\Omega_c$  is a volume bounded by polygons, so-called *faces*. A global set of faces  $F_h$  is defined, and each face is a sequence of *indices* of points in  $P_h$ . In this context, we define a cell set  $C_c$  as a set of indices of faces in the set of mesh faces  $F_h$ . Therefore, when referring to a volume defined by the cell, we use  $\Omega_c$  and its magnitude is then  $|\Omega_c|$ , and when we refer to the cell as an unordered index set, we use  $C_c$  and its magnitude  $|C_c|$  is the number of faces that bound the cell.

Solutions of continuum mechanical problems in geometrically complex solution domains significantly benefit from unstructured meshes. For example, gradients of solution variables are resolved at geometrically complex boundaries by employing mesh boundary layers, strongly reducing the number of cells required to achieve specific accuracy. Hence, this approx reduces the overall required computational resources.

As the phase indicator  $\chi(\mathbf{x}, t)$  given by eq. (1) contains a jump discontinuity, it poses difficulties for numerical simulations of two-phase flows. With Volume of fluid (VOF) methods, this non-continuous description is discretized by introducing the so-called *volume fraction*

$$\alpha_c = \frac{1}{|\Omega_c|} \int_{\Omega_c} \chi(\mathbf{x}, t) dx. \quad (3)$$

The unstructured VOF methods [30] rely on the volume fraction field  $\alpha_c$  to track interface with the advecting velocity obtained from the solution of two-phase Navier-Stokes equations in a single-field formulation. All multiphase flow simulation methods that utilize the single-field formulation of Navier-Stokes equations approximate the phase-indicator function similarly to eq. (3). The phase-indicator approximation utilizes signed distances in the Level Set [48, 47, 49] method, the volume fractions approximate the phase indicator for the Volume-of-Fluid [8, 37, 17, 40] method.

Various methods exist that compute the volume fraction  $\alpha_c$  based on the exact phase indicator  $\chi(\mathbf{x}, t)$ . The majority of methods calculate the integral in eq. (3) numerically, as schematically shown in fig. 2, using numerical quadrature.

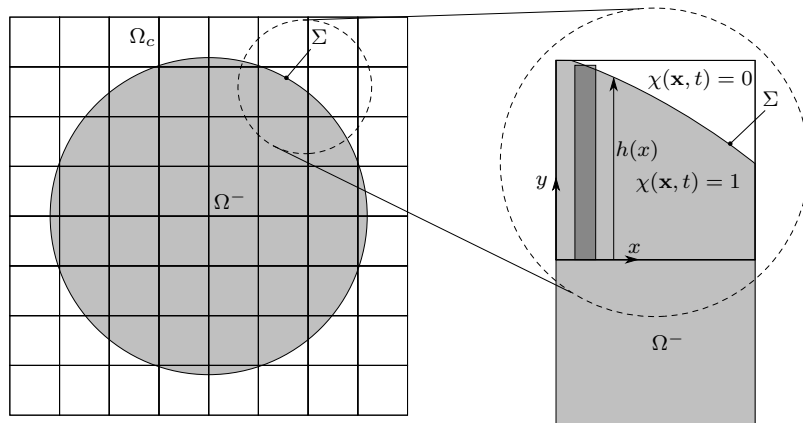


Figure 2: Calculating volume fractions of a circular interface by numerical integration.

Different approaches are outlined below with increasing complexity in terms of admissible shapes of the fluid interface. The admissible shapes range from analytic descriptions of basic geometric shapes such as spheres and ellipsoids to implicit functions (or their combinations) and more general shapes approximated with volume meshes.

Strobl et al. [46] propose an exact intersection between a sphere and a tetrahedron, a wedge, or a hexahedron. The proposed algorithm is exact and fast, though it is limited to the spherical interface shape.

Fries and Omerović [13] represent the fluid interface as a level set and propose a higher-order quadrature for the integral on the right-hand side of eq. (3). The parametrization of the surface uses roots of the implicit function found by the closest-point algorithm. Results are presented for hexahedral and tetrahedral unstructured meshes that may also be strongly deformed. Fries and Omerović [13, fig. 52, fig. 53] also show results with higher-order ( $> 2$ ) convergence for the volume integration of an arbitrary non-linear function on hexahedral and tetrahedral meshes. However, the volume and area integration error is reported for a single function. While a relative global volume error between  $1e-08$  and  $1e-06$  is reported, no information about the required CPU times is provided. In the approach proposed by Fries and Omerović [13], fluid interfaces with complex shapes are modeled as a composition of implicit functions.

Kromer and Bothe [25] propose an efficient third-order accurate quadrature for the eq. (3). Contrary to Jones et al. [21], who decompose cells into tetrahedrons, Kromer and Bothe [25] locally approximate the hypersurface by a paraboloid based on the principal curvatures. Applying the Gaussian divergence theorem to eq. (3) then yields contributions from the cell boundary and the approximated hypersurface patch. Using the surface divergence theorem, Kromer and Bothe [25] reformulate the contribution from the hypersurface patch into a set of line integrals, where the associated integrand emerges from the solution of a Laplace-Beltrami-type problem. The method of Kromer and Bothe [22] is directly applicable to unstructured meshes. However, locally, i.e., within a cell, the fluid interface must be  $C^2$  and simply connected.

Aulisa et al. [3] and Bnà et al. [5, 6] calculate the volume fraction by representing the indicator function as a height function inside cubic cells, using the structure of the underlying Cartesian mesh. Numerical integration of the height function is illustrated by fig. 2. However, extending this approach to unstructured meshes raises many questions. First, constructing a height function in a specific direction is complex and computationally expensive [38]. Second, the orientation of the interface in the chosen coordinate system may easily make the problem ill-conditioned. Finally, required mesh-search operations are complicated as the face normals of polyhedral cells are typically not aligned with the coordinate axes.

The calculation of the volume fraction given by  $\alpha_c = \frac{|\Omega^- \cap \Omega_c|}{|\Omega_c|}$  can be reformulated into the integration of a function  $f = 1$  within  $\Omega^- \cap \Omega_c$ . Since  $\partial\Omega_c$  consists of piecewise-planar surfaces (faces), the complexity lies in the non-planar part of the surface  $\partial\Omega^- \cap \Omega_c = \Sigma(t) \cap \Omega_c$ . Trimmed isogeometric analysis can be used to integrate  $f = 1$  within  $\Omega^- \cap \Omega_c$  by representing  $\partial\Omega^- \cap \Omega_c$  using a trimmed NURBS surface, effectively resulting in  $\alpha_c = \frac{|\Omega^- \cap \Omega_c|}{|\Omega_c|}$  for complex non-linear CAD surfaces. Although not yet applied to volume fraction calculation ( $f = 1$  integration), trimmed isogeometric analysis has been applied to solving PDEs in solution domains bounded by NURBS surfaces [24, 43, 36]. Similarly, the immersed isogeometric analysis (e.g. [11]) requires function integration in cut cells, where the integration of  $f = 1$  in the cut cell is equivalent to computing  $|\Omega^- \cap \Omega_c|$  used in volume fraction calculation. Although it is a potentially interesting alternative approach for computing volume fractions from CAD surfaces, the isogeometric analysis requires NURBS trimming, octree refinement, and higher-order quadratures. These efforts are worthwhile for the goal of achieving higher-order solutions for PDEs in complex solution domains. However, as demonstrated in the results section, our proposed algorithms achieve sufficient accuracy for signed distances and volume fractions on unstructured meshes while relying on straightforward second-order accurate discretization.

The signed distances in the Level Set Method require re-distancing (correction). The re-distancing methods are usually based on approximate solutions of Partial Differential Equations (PDEs) that ensure the signed-distance property [41]. Contrary to this approach, the unstructured Level Set / Front Tracking method [28, 51] *geometrically* computes minimal signed distances from  $\tilde{\Sigma}$ . This calculation is relatively straightforward on structured meshes [44, 45], but significantly more complex on unstructured meshes [28, 51]. Here we significantly extend the calculation of signed distances from [28, 51] by introducing an efficient approximate propagation of the inside/outside information from  $\tilde{\Sigma}$ .

Volume fraction calculation methods outlined so far model the fluid interface using exact functions and handle more complex interface shapes via combinations of these functions. A combination of exact functions cannot accurately capture the shape of the fluid interface in many cases. For example, when the interface shape is prescribed experimentally Hartmann et al. [16].

One approach exists that can handle arbitrarily complex interface shapes. In this approach, the fluid interface encloses a volumetric mesh as its boundary surface mesh. This mesh given by the fluid interface is intersected with a "background" mesh that stores volume fractions. This approach is called *volume mesh intersection*. An example for such an intersection between  $\tilde{\Omega}$  and cells from  $\tilde{\Omega}^-$  is shown in fig. 3. In principle, this approach is relatively straightforward, provided an accurate geometrical intersection of tetrahedrons is available. However, geometrical operations based on floating-point numbers are not stable and can lead to severe errors [52, chap. 45].

Ahn and Shashkov [1] have initialized volume fractions by volume mesh intersection as shown in fig. 3. In this approach, the approximated phase  $\tilde{\Omega}^-(t)$  is decomposed into volumes (an unstructured

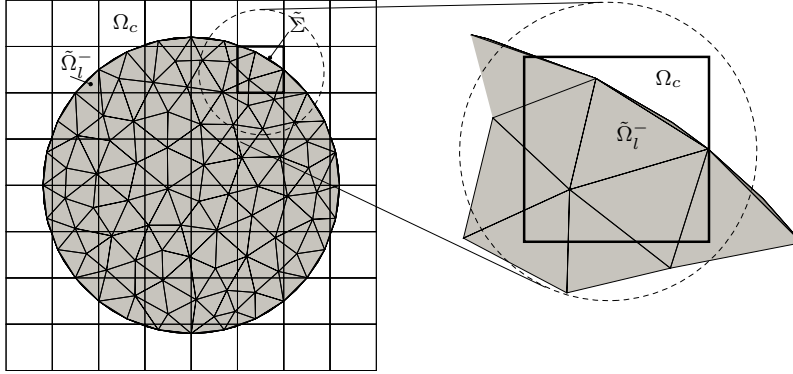


Figure 3: Calculating volume fractions from a circular interface by volume mesh intersection.

mesh), equivalently to the decomposition  $\tilde{\Omega}$  given by eq. (2). The boundary  $\partial\Omega^-$  is the fluid interface  $\Sigma(t)$ , and it is approximated as a polygonal surface mesh, leading to

$$\Omega^- \approx \tilde{\Omega}^- := \{\tilde{\Omega}_l^-\}_{l \in L}, \quad (4)$$

i.e. an approximation of  $\Omega^-$ . Generally, as shown in the detail in fig. 3, a cell  $\Omega_c$  of the background mesh  $\tilde{\Omega}$  may overlap with multiple cells  $\tilde{\Omega}_l^-$  from the  $\tilde{\Omega}^-$  mesh, and vice versa. We define a set of indices  $l$  of cells  $\tilde{\Omega}_l^-$  in  $\tilde{\Omega}^-$  that overlap with the cell  $\Omega_c$ : the so-called *cell stencil* of  $\Omega_c$  in  $\tilde{\Omega}_l^-$ , namely

$$\mathcal{S}(\Omega_c, \tilde{\Omega}^-) = \{l \in L : \Omega_c \cap \tilde{\Omega}_l^- \neq \emptyset, \text{ where } \Omega_c \in \tilde{\Omega}, \tilde{\Omega}_l^- \in \tilde{\Omega}^-\}, \quad (5)$$

where  $L$  is an index set, containing indices of cells from  $\tilde{\Omega}^-$ . Volume fractions  $\{\alpha_c\}_{c \in C}$  can then be calculated by performing the intersection

$$\alpha_c = \frac{|\cup_{l \in \mathcal{S}(\Omega_c, \tilde{\Omega}^-)} \Omega_c \cap \tilde{\Omega}_l^-|}{|\Omega_c|}. \quad (6)$$

Since each  $\tilde{\Omega}_l^-$  overlaps with at least a one cell from  $\tilde{\Omega}$ , and we can approximate the number of cells from  $\tilde{\Omega}$  that intersect each cell from  $\tilde{\Omega}^-$  as

$$N(\tilde{\Omega}^-, \tilde{\Omega}) \approx |\tilde{\Omega}^-| \text{mean}_{l \in L}(|\mathcal{S}(\tilde{\Omega}_l^-, \tilde{\Omega})|), \quad (7)$$

where  $|\tilde{\Omega}^-|$  denotes the number of cells in the mesh  $\tilde{\Omega}^-$ . The average number of cells  $\Omega_c$  overlapping  $\tilde{\Omega}_l^-$ ,  $\text{mean}_{l \in L}|\mathcal{S}(\tilde{\Omega}_l^-, \tilde{\Omega})|$ , depends on the mesh densities of both meshes,  $\tilde{\Omega}$  and  $\tilde{\Omega}^-$ . However, we do know that  $\text{mean}_{l \in L}|\mathcal{S}(\tilde{\Omega}_l^-, \tilde{\Omega})| > 1$ . Next, we know that  $|\tilde{\Omega}^-|$  grows quadratically in  $2D$  and cubically in  $3D$  with a uniform increase in mesh resolution, taken as the worst case scenario. It grows linearly in  $2D$  and quadratically in  $3D$  if  $\tilde{\Omega}^-$  is refined only near the interface  $\tilde{\Sigma} := \partial\tilde{\Omega}^-$ . Consequently, the computational complexity of the volume mesh intersection algorithm in terms of cell/cell intersections is quadratic in  $2D$  and cubic in  $3D$  in the worst case, and linear in  $2D$  and quadratic in  $3D$  if local refinement is used to increase the resolution of  $\tilde{\Sigma}$ . The quadratic complexity in  $3D$  is a serious drawback of this algorithm, especially for large simulations where  $|\tilde{\Omega}^-|$  easily reaches hundred

thousand cells per CPU core. Menon and Schmidt [34] have extended the volume mesh intersection algorithm from Ahn and Shashkov [1] to perform a volume conservative remapping of variables in the collocated Finite Volume Method (FVM) with second-order accuracy on unstructured meshes. Their results confirm the polynomial computational complexity in terms of absolute CPU times for this volume mesh intersection algorithm [34, table 3].

López et al. [26] propose a volume truncation algorithm for non-convex cells and apply it to the initialization of volume fractions from exact functions on unstructured meshes. Cell-subdivision is introduced to handle cases for which the interface crosses an edge of a cell twice. Non-planar truncated volumes are triangulated [26, fig 18], and second-order accuracy is demonstrated in terms of the relative global volume error for a uniform resolution and a higher-order accuracy when locally refined sub-grid meshes are used.

Ivey and Moin [18] initialize volume fractions on unstructured meshes using tetrahedral decomposition of non-convex cells and perform geometrical intersections with a similar approach as the approach from Ahn and Shashkov [1]. Unlike Ahn and Shashkov [1], Ivey and Moin [18] compute volume fractions of intersected tetrahedrons by intersecting them with exact signed distance functions that are used to model the fluid interface. Therefore, this algorithm cannot directly utilize arbitrarily shaped interfaces. However, their approach utilizes a linear interpolation of intersection points between the tetrahedron and the signed-distance function and yields second-order accuracy. Accuracy is further increased using adaptive mesh refinement.

The approaches reviewed so far require an exact representation of the interface using explicit analytic expressions, which hinders the direct application of such algorithms to initial conditions resulting from experiments as these are typically not available as function compositions. The volume mesh intersection algorithm [1] is flexible but computationally expensive, and it requires highly accurate and robust geometrical intersections.

The following sections outline the proposed algorithm that uses an unstructured surface mesh  $\tilde{\Sigma}$  to compute signed distances and volume fractions on unstructured meshes. Relying on unstructured surface meshes retains the ability to handle arbitrary-shaped surfaces while avoiding computationally expensive cell/cell intersections. Of course, using surface meshes to approximate the fluid interface renders the proposed algorithm second-order accurate; however, sufficient absolute accuracy is achievable with second-order accurate methods using local mesh refinement on the background mesh [7, 12]. Applying local mesh refinement on the background mesh in the close vicinity of the triangulated surface increases the accuracy and limits it to the resolution of the surface mesh, not the background mesh that stores volume fractions and signed distances. The proposed algorithm geometrically computes signed distances near the fluid interface. These signed distances (so-called *narrow-band* signed-distances) are then propagated throughout  $\tilde{\Omega}$  by an approximate solution of a diffusion equation. The propagated signed distances determine the value of the phase indicator  $\chi(\mathbf{x}, t)$  in those cells that are either completely empty ( $\alpha_c = 0$ ), or completely full ( $\alpha_c = 1$ ). Finally, second-order accurate volume fraction values are calculated in intersected cells ( $0 < \alpha_c < 1$ ). This work enables the calculation of complex initial conditions for different multiphase simulation methods. These include in particular geometric [20, 18, 39, 29, 42] and algebraic VOF methods [54, 9]. The calculation of volume fractions from a surface mesh (marker points in 2D) was done in the mixed markers / VOF method by Aulisa et al. [2]: the proposed algorithm significantly extends this idea towards an accurate and fast volume fraction model for Front Tracking methods [53], as well as the hybrid Level Set / Front Tracking methods on structured [44, 45] or unstructured [28, 51] meshes. Signed distances and the respective inside-outside information from triangulated surfaces are available for unstructured Level Set and Immersed Boundary methods.

## 2. Surface mesh / cell intersection algorithm

The calculation of volume fractions by the proposed Surface Mesh Cell Intersection/Approximation (SMCI/A) algorithm, outlined in fig. 4, requires signed distances to the interface at cell centres and cell corner points. As a naive computation is computationally expensive (section 2.2), we employ an octree based approach to the calculation of signed distances. Starting point of the octree based search is the calculation of search radii at the relevant points.

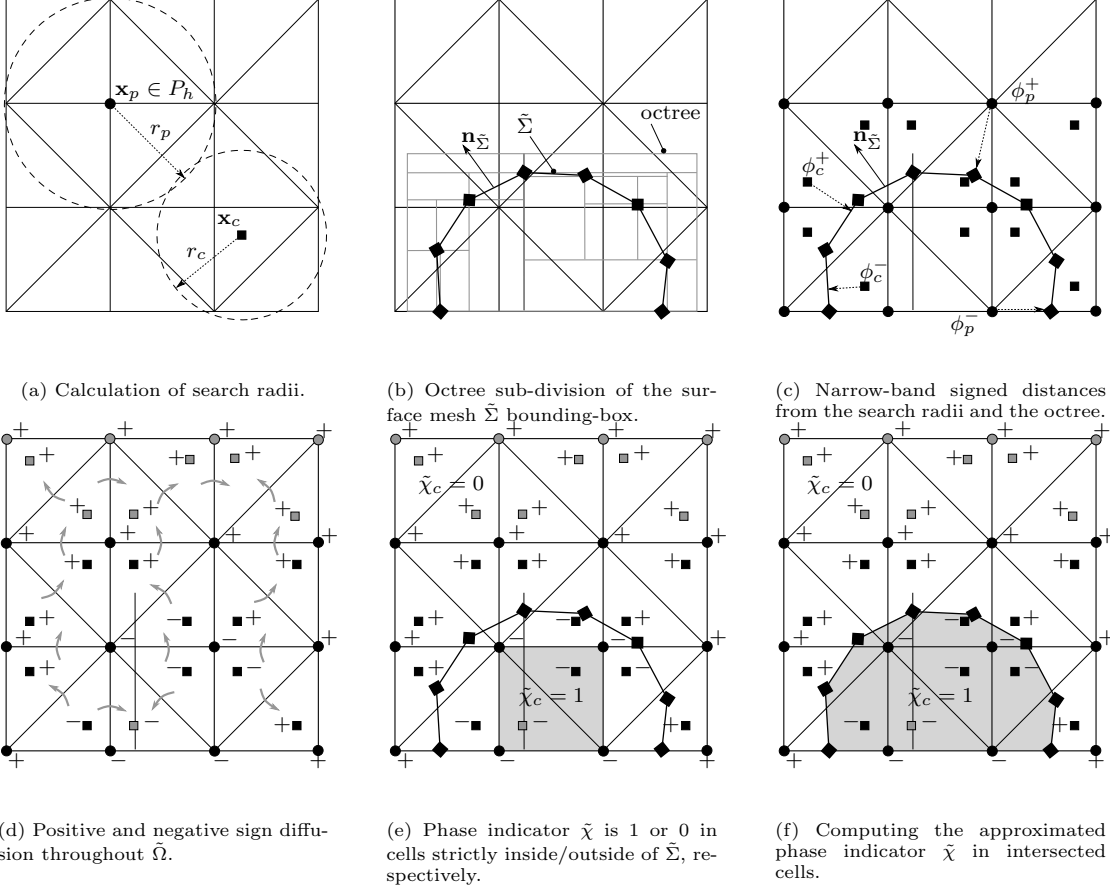


Figure 4: Steps of the Surface Mesh Intersection / Approximation (SMCI/A) algorithms.

### 2.1. Calculation of search radii

In the first step, a search radius  $r_c$  and  $r_p$  is calculated at each cell center and cell-corner point, respectively. This is illustrated in fig. 4a. Here, the cell search radius  $r_c$  is defined by

$$r_c = \lambda_s \min_{f \in F_c} \|\mathbf{x}_{f,O} - \mathbf{x}_{f,N}\|_2, \quad (8)$$

where  $\mathbf{x}_c$  is the cell center,  $\lambda_s > 0$  is the *search radius factor* detailed below and  $\mathbf{x}_{f,O}$ ,  $\mathbf{x}_{f,N}$  are the cell centers of two cells that share the face with index  $f$  of the cell  $\Omega_c$  ( $O$  for owner cell with

a smaller cell index than the neighbor cell  $N$ ). Here, the index set  $F_c$  contains the indices of those faces that form the boundary of  $\Omega_c$ . Based on (8), the corner-point search radius  $r_p$  is defined by

$$r_p = \lambda_s \min_{c \in C_p(\mathbf{x}_p)} r_c, \quad (9)$$

where  $\mathbf{x}_p$  is the cell-corner point, while the *point-cell stencil* is the index set  $\mathcal{S}(\mathbf{x}_p, \tilde{\Omega})$ , that contains indices of all cells from  $\tilde{\Omega}$  whose corner-point is  $\mathbf{x}_p$ .

The search radii introduced above are used to define search balls in  $3D$  (circles in  $2D$ ), which are used to reduce the number of calculations to determine signed distances between the cell corner points  $\mathbf{x}_p$  and the cell centers  $\mathbf{x}_c$  with respect to the provided surface mesh  $\tilde{\Sigma}$ .

## 2.2. Octree decomposition of the surface mesh and signed distance calculation

In contrast to various other approaches for volume fraction initialization, the fluid interface is not represented by the proposed algorithm using a function, but as a surface mesh, consisting of triangles. To define the interface  $\tilde{\Sigma}$ , we first denote the convex hull of a set of  $n$  points  $P^n = \{\mathbf{x}_1, \dots, \mathbf{x}_n\}$ ,  $\mathbf{x}_i \in \mathbb{R}^3$  by

$$\text{conv}(P^n) := \left\{ \mathbf{x} \in \mathbb{R}^3 : \mathbf{x} = \sum_{\mathbf{x}_i \in P^n} \gamma_i \mathbf{x}_i, \sum_{i=1}^n \gamma_i = 1 \right\}. \quad (10)$$

Using this, a triangle is defined as the convex hull of a point triple:  $\mathcal{T} := \text{conv}(P^3)$ . Consequently, the surface mesh is defined as

$$\tilde{\Sigma} := \{\mathcal{T}_1, \mathcal{T}_2, \dots, \mathcal{T}_n\}. \quad (11)$$

With the structure of  $\tilde{\Sigma}$  in mind, we want to emphasize why an octree based approach is the key to obtaining reasonable computation times. Consider the case where a minimal distance between a point  $\mathbf{x}$  and  $\tilde{\Sigma}$  would be calculated for each cell center  $\mathbf{x}_c$  and cell-corner point  $\mathbf{x}_p$ . The need for the spatial subdivision and search operations becomes obvious, as this would require a distance computation between each point of the interface mesh and each cell centers and cell corner points of the background mesh. Consequently, this would require  $|C| |\tilde{\Sigma}|$  operations to compute the geometric signed distances at cell centers and additional computations for evaluating signed distances at cell-corner points. For our computations below, the number  $|C|$  often reaches the order of  $1e05$  per CPU core, while  $|\tilde{\Sigma}|$  is typically on the order of  $1e04$  per CPU core. Aiming at redistancing computations for a dynamic setting in multiphase flows where  $\tilde{\Sigma} = \tilde{\Sigma}(t)$ , such a large number of distance computations makes such a brute force redistancing approach prohibitively expensive.

The first step of the signed distance calculation is the computation of an Axis-Aligned Bounding Box (AABB) from the surface mesh  $\tilde{\Sigma}$ . The AABB is used to build an octree data structure, illustrated as a  $2D$  quadtree subdivision in fig. 4b, which is used to access  $\tilde{\Sigma}$ . The octree data structure enables fast search queries involving cell centers and cell corner-points that are close to the surface mesh  $\tilde{\Sigma}$ , with a logarithmic computational complexity with respect to the number of vertices in  $\tilde{\Sigma}$  [32, 33]. The structure of the octree depends on the ordering of vertices in  $\tilde{\Sigma}$ : since  $\tilde{\Sigma}$  is an unstructured surface mesh, its vertices are generally sufficiently unordered, which makes the octree well-balanced. Once the octree has been constructed, it can be used to find the closest points  $\mathbf{x} \in \tilde{\Sigma}$  to cell centres  $\mathbf{x}_c$  and cell corner points  $\mathbf{x}_p$ . Note that this is only true for those  $\mathbf{x}_c, \mathbf{x}_p$  which are sufficiently close to  $\tilde{\Sigma}$  in terms of their search radius  $r_c, r_p$ . Thus, the search radii define a so-called *narrow band* around  $\tilde{\Sigma}$ , where the nearest distances are calculated geometrically. We

denote the narrow band of  $\tilde{\Sigma}$  with  $\mathcal{N}(\tilde{\Sigma})$ , and the closed ball  $\mathcal{B}(\mathbf{x}^*, r) := \{\mathbf{x} \in \mathbb{R}^3 \mid \|\mathbf{x} - \mathbf{x}^*\|_2 \leq r\}$  with a radius  $r$  around a point  $\mathbf{x}$ . Then

$$\mathcal{N}(\tilde{\Sigma}) := \left\{ \mathbf{x} \in \mathbb{R}^3 \mid \exists \mathcal{T} \in \tilde{\Sigma} \text{ such that } \mathcal{T} \cap \mathcal{B}(\mathbf{x}, r) \neq \emptyset \right\}, \quad (12)$$

where  $r$  is either  $r_p$  or  $r_c$ .

For a point  $\mathbf{x} \in \mathcal{N}(\tilde{\Sigma})$ , the octree provides the closest point  $\mathbf{x}_{\min} \in \mathcal{T}_{\min}$  for some  $\mathcal{T} \in \tilde{\Sigma}$  and the corresponding triangle  $\mathcal{T}_{\min}$  itself. While the absolute distance can be directly computed as  $\|\mathbf{x} - \mathbf{x}_{\min}\|_2$ , care must be taken when computing the sign with respect to the orientation of  $\tilde{\Sigma}$ . Directly using the triangle normals  $\mathbf{n}_{\mathcal{T}}$  may lead to false signs and consequently, to erroneous volume fractions. Thus, we follow the work of [50, 4] and compute *angle weighted normals*

$$\mathbf{n}_{\mathbf{x}_v} = \frac{\sum_{\mathcal{T} \in \text{ngh}(\mathbf{x}_v)} \beta_{\mathcal{T}} \mathbf{n}_{\mathcal{T}}}{\sum_{\mathcal{T} \in \text{ngh}(\mathbf{x}_v)} \beta_{\mathcal{T}}} \quad (13)$$

at the vertices  $\mathbf{x}_v$  of  $\tilde{\Sigma}$ . Here,  $\text{ngh}(\mathbf{x}_v)$  denotes the set of all triangles containing  $\mathbf{x}_v$ ,  $\mathbf{n}_{\mathcal{T}}$  a triangle normal and  $\beta_{\mathcal{T}}$  the inner angle of  $\mathcal{T}$  at  $\mathbf{x}_v$ . Baerentzen and Aanaes [4] propose a classification of the point  $\mathbf{x}_{\min}$  whether it is located within a triangle, on an edge, or a vertex and base the choice of the normal on this classification. While such a classification is simple in theory, a robust implementation is difficult due to the limited precision of floating point arithmetic. Thus, we opt for a linear interpolation of  $\mathbf{n}_{\mathbf{x}_v}$  within  $\mathcal{T}_{\min}$  to  $\mathbf{x}_{\min}$ , denoted  $\mathbf{n}_I(\mathbf{x}_{\min}, \mathcal{T}_{\min})$ . With this normal computation, the signed distance between  $\mathbf{x}$  and  $\mathbf{x}_{\min}$  is calculated by

$$\phi^g(\mathbf{x}, \tilde{\Sigma}) = \text{sign}((\mathbf{x} - \mathbf{x}_{\min}) \cdot \mathbf{n}_I(\mathbf{x}_{\min}, \mathcal{T}_{\min})) \|\mathbf{x} - \mathbf{x}_{\min}\|_2. \quad (14)$$

where the supindex  $g$  indicates a geometrical construction. This procedure is illustrated in fig. 4c. The robustness of this approach with regard to inside/outside classification is demonstrated in section 4.3.

Using the spatial subdivision provided by the octree, the computational complexity for finding the minimal distances between mesh points and  $\tilde{\Sigma}$  is reduced severely, as the vast majority of cell centers  $\mathbf{x}_c$  are not even considered for calculation as no triangle  $\mathcal{T} \in \tilde{\Sigma}$  exists within the corresponding search ball. The closest triangles of those points  $\mathbf{x}_c$ , whose ball  $\mathcal{B}(\mathbf{x}_c, r_c)$  intersects  $\tilde{\Sigma}$  are found with logarithmic search complexity with respect to  $|\tilde{\Sigma}|$ . This significant reduction of complexity can potentially enable a future application of the proposed algorithm on moving interfaces  $\tilde{\Sigma}(t)$  as a geometrically exact marker field model for unstructured Front Tracking methods. Therefore, it is crucial to understand that the  $\min_{\mathcal{T} \in \tilde{\Sigma}}$  operation in eq. (14) throughout this text relies on the octree spatial subdivision and search queries.

### 2.3. Signed distance propagation

After the calculation of geometric signed distances in the narrow band around  $\tilde{\Sigma}$ , the signed distances are propagated to the bulk of different phases, as shown in fig. 4d. In [28, 51], the geometric signed distances are set to large positive numbers throughout the domain, and a graph-traversal algorithm is used to iteratively correct the signs of signed distances using face-cell and point-point graph connectivity provided by the unstructured mesh. Graph-traversal is computationally expensive and complicated to implement in parallel. Here we propose a straightforward alternative that

instantaneously propagates signs of signed distances through the solution domain and is parallelized easily. We rely on the diffusion equation for the signed distances, namely

$$\begin{aligned} -\Delta\phi &= 0, \\ \nabla\phi &= 0, \quad \text{for } \mathbf{x} \in \partial\Omega \end{aligned} \tag{15}$$

and its discretization using the unstructured finite volume method in OpenFOAM [19, 23, 35], giving a linear system of equations. The key idea to sign propagation is to apply a few iterations ( $< 5$ ) of an iterative linear solver to this system. In our case a Conjugate Gradient approach with an incomplete lower upper preconditioner has been used. With the initial field set to

$$\phi(\mathbf{x}) = \begin{cases} \phi_g(\mathbf{x}, \tilde{\Sigma}), & \text{if } \mathbf{x} \in \mathcal{N}(\tilde{\Sigma}) \\ 0, & \text{otherwise,} \end{cases} \tag{16}$$

this small number of iterations suffices to properly propagate  $\text{sign}(\phi)$  with respect to the orientation of  $\tilde{\Sigma}$  throughout  $\tilde{\Omega}$ . Prerequisite for this approach to work is that the narrow band has a certain minimum width in interface normal direction. At least four cells on each side of the interface are required to ensure a robust propagation. This is achieved by setting a global search radius factor  $\lambda_s := 4$  in eq. (8) used to calculate  $r_c$  at cell centers. Note that increasing  $\lambda_s$  beyond this value only increases computational costs, and does not impact the accuracy of the proposed algorithm, as with a larger value of  $\lambda_s$  the narrow band  $\mathcal{N}(\Sigma)$  becomes wider and consequently the geometrical signed distances are calculated at more points  $\mathbf{x}_c, \mathbf{x}_p$ , using eqs. (17) and (20), respectively.

Two aspects have to be considered when solving the linear system of equations resulting from the discretization of eq. (15). First, cells for which  $\mathbf{x}_c \in \mathcal{N}(\tilde{\Sigma})$  have to be excluded from the vector of unknowns as  $\phi^g(\mathbf{x}_c)$  is already known for those. Second, for cells away from  $\mathcal{N}(\tilde{\Sigma})$  the only relevant information is  $\text{sign}(\phi_c)$  indicating  $\Omega_c \in \Omega^-$  or  $\Omega_c \in \Omega^+$ , respectively. A few iterations of a linear solver suffice to reliably propagate  $\text{sign}(\phi_c)$  to the entire domain. The resulting field is

$$\phi_c = \begin{cases} \phi_c^g, & \text{if } \mathbf{x}_c \in \mathcal{N}(\tilde{\Sigma}), \\ \phi_c^a, & \text{otherwise,} \end{cases} \tag{17}$$

with  $\phi_c^g$  denoting geometric signed distances and  $\phi_c^a$  approximate values from the solution of eq. (15) carrying inside/outside information but without geometric meaning.

Once the cell-centered signed distances  $\phi_c$  are computed, they are used to calculate the signed distances at cell corner-points via

$$\phi_p^I = \sum_{c \in C_p} w_{p,c} \phi_c, \tag{18}$$

where  $C_p$  is the index set of cells that contain the cell corner point  $\mathbf{x}_p$  and the supindex  $I$  indicating interpolation. Furthermore,  $w_{p,c}$  is the *inverse-distance weighted* (IDW) interpolation weight

$$w_{p,c} = \frac{\|\mathbf{x}_c - \mathbf{x}_p\|_2^{-1}}{\sum_{\tilde{c} \in C_p} \|\mathbf{x}_{\tilde{c}} - \mathbf{x}_p\|_2^{-1}}. \tag{19}$$

As with  $\phi_c$ , the accuracy of  $\phi_p$  is irrelevant outside of the narrow band of  $\tilde{\Sigma}$ , only the sign of the signed distance is important in the bulk. To correct for the error introduced by the IDW-interpolation in eq. (18), signed distances at cell-corner points of intersected cells are calculated

geometrically

$$\phi_p = \begin{cases} \phi_p^g, & \text{if } \mathbf{x}_p \in \mathcal{N}(\tilde{\Sigma}), \\ \phi_p^I, & \text{otherwise.} \end{cases} \quad (20)$$

Equations (17) and (20) define the final signed distances at cell centers and cell-corner points, respectively. These quantities will have the value of a geometrical distance to  $\tilde{\Sigma}$  in the narrow band, while outside of the narrow band only the correct sign resulting from the approximative solution of eq. (15) is relevant.

#### 2.4. Volume fraction calculation

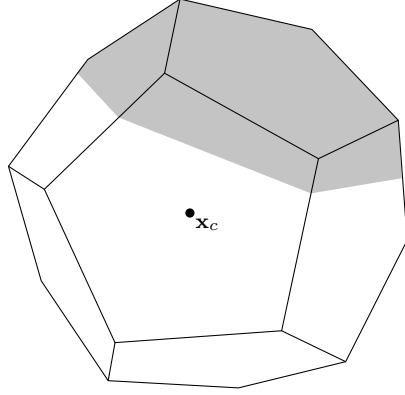
Once the signed distances at cell centers  $\{\phi_c\}_{c=1,2,\dots,|\tilde{\Omega}|}$  and cell corner points  $\{\phi_p\}_{p=1,2,\dots,|P_h|}$  are calculated as outlined in the previous section, the SMCI algorithm calculates the volume fractions in a straightforward way. The volume fraction calculation is shown schematically for the SMCI algorithm in fig. 5b. Each cell is decomposed into tetrahedrons, using the cell centroid  $\mathbf{x}_c$  as the base point of the tetrahedron, the centroid of the face  $\mathbf{x}_{c,f}$ , and two successive points from the cell-face,  $\mathbf{x}_{c,f,i}, \mathbf{x}_{c,f,i+1}$ . The resulting tetrahedron has the distance  $\phi_c$  associated to the cell centroid, the distance  $\phi_{c,f}$  associated to the face centroid, and and  $(\phi_{c,f,i}, \phi_{c,f,i+1})$  pair of distances associated with a pair of points that belong to the cell-face  $(c, f)$ , as shown in fig. 5b. If all the distances of the tetrahedron are negative, the tetrahedron lies in the negative halfspace with respect to  $\tilde{\Sigma}$ , and its total volume contributes to the sum of the volume of phase 1 inside the volume  $\Omega_c$ . If a pair of distances in a tetrahedron has different signs, the tetrahedron is intersected by the interface approximated by the surface mesh  $\tilde{\Sigma}$ . The volume of this intersection is calculated by geometrically intersecting the tetrahedron with those triangles from  $\tilde{\Sigma}$ , that have a non-zero intersection with a ball  $\mathcal{B}$  enclosing the tetrahedron. The center of the ball  $\mathcal{B}_{c,f,i} := \mathcal{B}(\mathbf{x}_{c,f,i}, R_{c,f,i})$  is the centroid of the tetrahedron  $\mathbf{x}_{c,f,i} = 0.25(\mathbf{x}_c + \mathbf{x}_{c,f} + \mathbf{x}_{c,f,i} + \mathbf{x}_{c,f,\text{mod}(i+1,|F_{c,f}|)})$ , where  $i = 0, \dots, |F_{c,f}| - 1$ , and  $F_f$  is the oriented set of indices of the points  $\mathbf{x}$  (cf. fig. 5b) that belong to the face  $f$  of the cell  $\Omega_c$ . The radius of the tetrahedron-ball  $\mathcal{B}_{c,f,i}$  is then

$$R_{c,f,i} = \max(\|\mathbf{x}_c - \mathbf{x}_{c,f,i}\|, \|\mathbf{x}_{c,f} - \mathbf{x}_{c,f,i}\|, \|\mathbf{x}_{c,f,j} - \mathbf{x}_{c,f,i}\|, \|\mathbf{x}_{c,f,\text{mod}(j+1,|F_{c,f}|)} - \mathbf{x}_{c,f,i}\|), \quad (21)$$

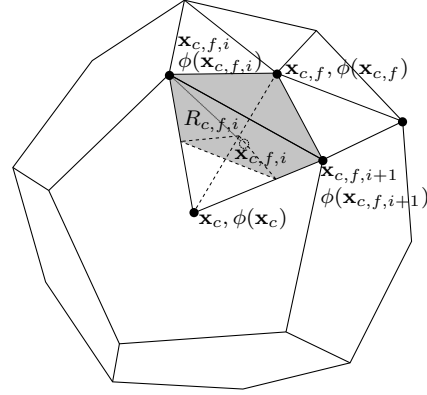
$j = 0, \dots, |F_{c,f}| - 1$ . This sub-set of  $\tilde{\Sigma}$  is found using the octree data structure with logarithmic complexity with respect to  $\tilde{\Sigma}$ , as outlined in the previous section. For the example tetrahedron in the cell shown in fig. 5b, the resulting intersection between the approximated interface  $\tilde{\Sigma}$  and a tetrahedron from the cell  $\Omega_c$  is shown as the shaded volume. The magnitude of this volume is computed by applying the Gauss divergence theorem using eq. (31). The phase-specific volumes from cell-tetrahedrons are summed up for the cell  $\Omega_c$ , into the total phase-specific volume of the phase 1 within the cell  $\Omega_c$ , and the volume fraction is therefore computed as

$$\alpha_c = \frac{\sum_{f=0,\dots,|C_c|-1} \sum_{i=0,\dots,|F_{c,f}|-1} |T(\mathbf{x}_c, \mathbf{x}_{c,f}, \mathbf{x}_{c,f,i}, \mathbf{x}_{c,f,\text{mod}(i+1,|F_{c,f}|)}) \cap (\mathcal{B}_{c,f,i} \cap \tilde{\Sigma})|}{|\Omega_c|} \quad (22)$$

with  $T := \{\mathbf{x}_1, \mathbf{x}_2, \mathbf{x}_3, \mathbf{x}_4\}$  denoting a tetrahedron. The SMCI algorithm is summarized by algorithm 1.



(a) A cell  $\Omega_c$  intersected by  $\tilde{\Sigma}$ .



(b) Tetrahedral cell decomposition.

Figure 5: Centroid decomposition of an interface cell into tetrahedra and calculation of  $\alpha_c$  using the SMCI/A algorithms.

---

**Algorithm 1** The Surface-Mesh / Cell Intersection Algorithm (SMCI)

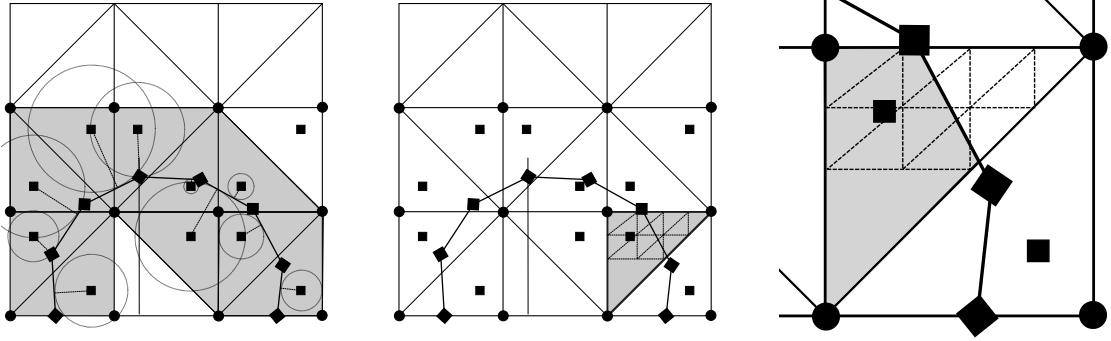
---

- 1:  $\alpha_c = 0, \phi_{c,p} = 0$
  - 2: Compute search radius for cell centers  $r_{c \in C}$  using eq. (8).
  - 3: **for** cell centroids  $\{\mathbf{x}_c\}_{c \in C}$  **do**
  - 4:   Place the vertices of  $\tilde{\Sigma}$  into an octree (section 2.2).
  - 5:   Find the triangle  $\mathcal{T}_n \in \tilde{\Sigma}$  nearest to  $\mathbf{x}_c$  within a ball  $\mathcal{B}(\mathbf{x}_c, r_c)$ .
  - 6:   Set  $\phi_c^g := \phi^g(\mathbf{x}_c, \mathcal{T}_n)$  using eq. (14).
  - 7: **end for**
  - 8: Approximately solve eq. (15) to propagate  $sign(\phi_c)$ .
  - 9: Compute search radius for cell corner points  $r_{p \in P}$  using eq. (9).
  - 10: Find all intersected cells  $I = \{c, \phi_c \phi_p < 0 \text{ for at least one } p\}$ .
  - 11: Use eq. (17) to correct  $\phi_c$  within the narrow band.
  - 12: Compute  $\phi_p$  in the bulk using eq. (18).
  - 13: Use eq. (20) to correct  $\phi_p$  within the narrow band.
  - 14: **for** cells  $\{\Omega_c\}_{c \in C}$  **do**
  - 15:   **if**  $\phi_c \leq 0$  and all corner-point distances  $\phi_p \leq 0$  **then**    $\triangleright$  Cell is inside the negative  $\tilde{\Sigma}$ -halfspace.
  - 16:      $\alpha_c = 1$
  - 17:   **end if**
  - 18:   **if** cell  $\Omega_c$  is intersected,  $c \in I$  **then**    $\triangleright$  Cell is intersected by  $\tilde{\Sigma}$ .
  - 19:      $\alpha_c$  given by eq. (22).
  - 20:   **end if**
  - 21: **end for**
- 

### 3. Surface-Mesh / Cell Approximation algorithm

This section presents an alternative approach to the computation of volume fractions presented in section 2.4. While section 2.4 details a method based on geometric intersections, this section introduces an algorithm based on volumetric reconstruction by adaptive mesh refinement. Detrixhe and Aslam [10] introduce a second order accurate approximation for the volume fraction of a triangle

(2D) or a tetrahedron (3D). Their model is an algebraic expression taking the signed distances  $\phi$  of the vertices as arguments. In contrast, we propose a volume fraction initialization algorithm that employs this model in combination with an adaptive tetrahedral cell decomposition and the octree-based signed distance calculation described in section 2. We term this algorithm *Surface-Mesh/Cell Approximation* (SMCA) and it is outlined below.



(a) Identify potential interface cells (marked grey) using bounding ball criterion. Shown are circles with radii  $|\phi_c|$ .

(b) Adaptive, tetrahedral decomposition of interface cells. Compute  $\phi$  at new vertices.

(c) Compute the volume fraction  $\alpha_c$  using the model of Detrixhe and Aslam [10] (detail view).

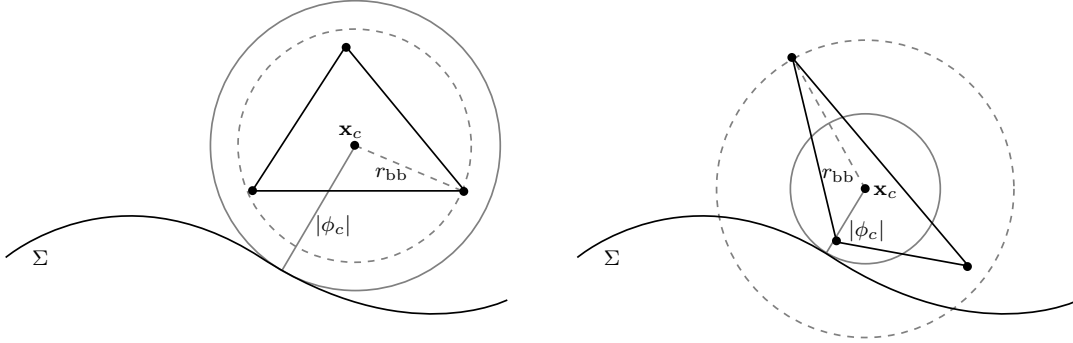
Figure 6: Steps of the SMCA algorithm following signed distance computation and inside/outside propagation.

The SMCA-algorithm is based on the signed distance results of the SMCI-algorithm introduced in section 2. The steps depicted in fig. 4a - 4d of the SMCI/A are used to compute  $\phi_c, \phi_p$  in the narrow band and propagate inside/outside information in the rest of the mesh points. Subsequent steps for the computation of volume fractions are displayed in fig. 6. First, all cells intersected by  $\tilde{\Sigma}$  are identified to reduce computational costs, as only these cells have intermediate values  $0 < \alpha_c < 1$ . This step is depicted in fig. 6a. Each cell for which  $\mathbf{x}_c \in \mathcal{N}(\tilde{\Sigma})$  is checked with the *bounding ball criterion*. We define a bounding ball (bb) for a point  $\mathbf{x}_{bb} \in \Omega_c$  using  $r_{bb} = \max_{\mathbf{x} \in \Omega_c} \|\mathbf{x} - \mathbf{x}_{bb}\|_2$ . This ball is the smallest ball that contains all points of  $\Omega_c$ . We compare this bounding ball to  $\mathcal{B}(\mathbf{x}_{bb}, |\phi(\mathbf{x}_{bb})|)$ . These balls are shown in fig. 7, where the bounding ball is illustrated by a dashed and the other ball by a continuous line. As a general observation, if the bounding ball is contained in the ball with the radius  $|\phi(\mathbf{x}_{bb})|$ , i.e.  $\mathcal{B}(\mathbf{x}_{bb}, r_{bb}) \subseteq \mathcal{B}(\mathbf{x}_{bb}, |\phi(\mathbf{x}_{bb})|)$ , then such a cell is guaranteed to be a bulk cell. This cell can then be removed from the set of cells in the narrow band to reduce the number of cells which are considered for decomposition in the next step. If the criterion is not satisfied, the cell is considered an interface cell. Two remarks on this criterion: first, the existence of such a  $\mathbf{x}_{bb}$  is not a necessary but a sufficient condition. Second, in a practical implementation evaluation of this criterion is only feasible for a small number of points when aiming to keep computational costs reasonable. Thus, the actual check is performed by evaluating

$$f_{bb}(\mathbf{x}, \phi_{\mathbf{x}}, \Omega_c) = \begin{cases} 1, & \max_{\mathbf{x}_i \in \Omega_c} \|\mathbf{x}_i - \mathbf{x}\|_2 \leq |\phi_{\mathbf{x}}|, \\ 0, & \text{otherwise} \end{cases} \quad (23)$$

with  $\mathbf{x} \in \Omega_c$ . The evaluation of the max-operator is based on a comparison to the corner points  $\mathbf{x}_i$  of the cell  $\Omega_c$ . For example, in our implementation this function is only evaluated at cell centres  $\mathbf{x}_c$

(original mesh cells, see below) or cell corner points (tetrahedra resulting from decomposition). As a consequence, a few bulk cells are considered as interface cells (fig. 7b). We deem this acceptable as this only has a minor impact on the computational time, but not on the computed volume fractions.



(a) Bulk cell: the ball  $\mathcal{B}(\mathbf{x}_c, |\phi_c|)$  contains the cell bounding ball  $\mathcal{B}(\mathbf{x}_c, r_{bb})$ .

(b) False positive: a bulk cell which is not detected by the bounding ball criterion as  $\mathcal{B}(\mathbf{x}_c, r_{bb}) \not\subseteq \mathcal{B}(\mathbf{x}_c, |\phi_c|)$ .

Figure 7: Illustration of the idea of the bounding ball criterion in 2D for clarity. The solid grey line represents  $\mathcal{B}(\mathbf{x}_c, |\phi_c|)$ , the grey dashed one  $\mathcal{B}(\mathbf{x}_c, r_{bb})$ .

After identification of interface cells, the cell volume fractions are initialized according to the sign of  $\phi_c$ ,

$$\alpha_c = \begin{cases} 1, & \phi_c \leq 0, \\ 0, & \text{otherwise.} \end{cases} \quad (24)$$

This gives correct volume fractions for bulk cells, while the values of interface cells are updated as described below. Each cell flagged as an interface cell by the method described above is decomposed into tetrahedra using its centroid and cell face centroids as shown in fig. 5. Each resulting tetrahedron is further refined in an adaptive manner such that resolution is only subsequently increased where a new tetrahedron is again intersected by the interface. To achieve this, a tetrahedron  $T$  is checked with the bounding ball criterion eq. (23). The criterion is only evaluated at the vertex  $\mathbf{x}_{\max} \in T$  for which  $|\phi(\mathbf{x}_{\max})| = \max_{\mathbf{x} \in T} |\phi(\mathbf{x})|$ . Only if  $f_{bb}(\mathbf{x}_{\max}, \phi, T) = 0$  (eq. (23)),  $T$  is considered for further decomposition. An obvious choice would be decomposition at the centroid of  $T$ . However, repeated application of this approach results in increasingly flattened tetrahedra. To avoid this problem, we apply the decomposition shown in fig. 8. First, from the vertices edge centres of the tetrahedron

$$\mathbf{x}_{ij} = \frac{1}{2}(\mathbf{x}_i + \mathbf{x}_j), \quad i, j \in \{1, 2, 3, 4\}, i \neq j \quad (25)$$

are computed (fig. 8a). By combining each vertex  $\mathbf{x}_i$  with the three edge centres of the adjacent edges, four new tetrahedra are created (fig. 8b). The remainder of the original tetrahedron is an octahedron (fig. 8b grey dashed lines) constituted by the edge centres  $\mathbf{x}_{ij}$ . This octahedron is decomposed into four additional tetrahedra by choosing two opposite edge centres as shown by the black line in fig. 8c. The indices of vertices of such a line are the numbers one to four. From the

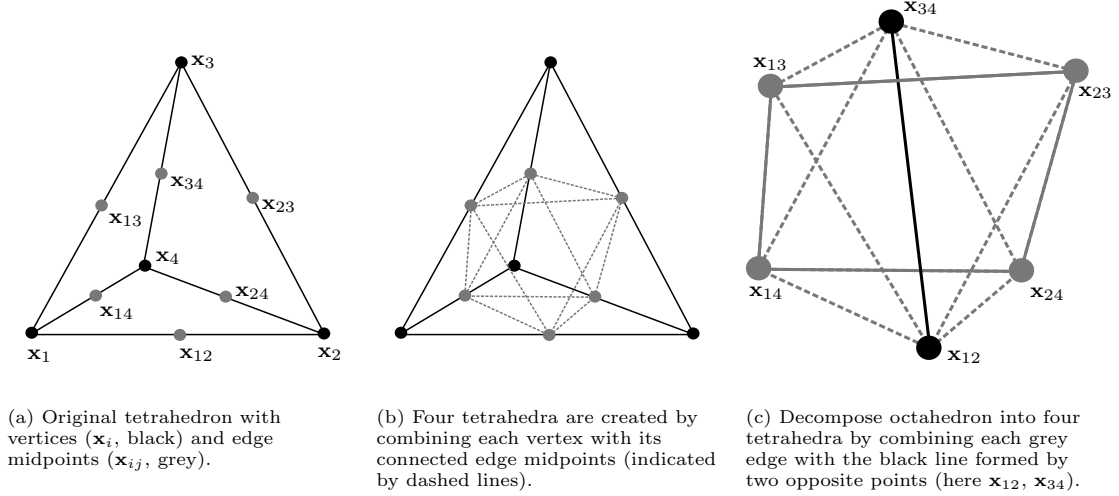


Figure 8: Decomposition of a tetrahedron into eight tetrahedra using edge midpoints.

remaining four edge centres, point pairs are created such that  $\{\mathbf{x}_{mn}, \mathbf{x}_{mo}\}$  or  $\{\mathbf{x}_{mn}, \mathbf{x}_{on}\}$ , yielding four pairs. Combining each pair with  $\{\mathbf{x}_{ij}, \mathbf{x}_{kl}\}$  (e.g. black edge in fig. 8c) gives the aforementioned four tetrahedra. Subsequently,  $\phi$  is computed for the added vertices  $\mathbf{x}_{ij}$ . The decomposition is based on the pair of edge centres that have the smallest distance between each other. Refinement is completed when a maximum refinement level  $l_{\max}$  is reached. This can either be an arbitrary prescribed value or can be computed such that the edge length of the refined tetrahedra is comparable to the edge length of surface triangles. In the latter case,

$$l_{\max} = \min_{l \in \mathbb{N}} \left( \frac{L_{\text{tet}}}{L_{\text{tri}}} < 2^l \right) \quad (26)$$

with  $L_{\text{tet}}$  and  $L_{\text{tri}}$  being cell specific reference lengths for tetrahedra and surface triangles, respectively. Different choices for  $L_{\text{tet}}$  and  $L_{\text{tri}}$  are possible. We choose

$$L_{\text{tet}} = \frac{1}{n_t} \sum_{\mathbf{e} \in E_{\text{cdc}}} |\mathbf{e}|,$$

$$L_{\text{tri}} = \min_{\mathbf{e} \in E_{\tilde{\Sigma}, c}} |\mathbf{e}|$$

with  $E_{\text{cdc}}$  denoting the set of edges resulting from tetrahedral decomposition of a cell  $\Omega_c$  at its centroid,  $n_t$  the number of edges in  $E_{\text{cdc}}$  and  $E_{\tilde{\Sigma}, c}$  a subset of edges of  $\tilde{\Sigma}$ . The set  $E_{\tilde{\Sigma}, c}$  consists of all edges of  $\mathcal{T} \in \tilde{\Sigma}$  for which  $\mathcal{T} \cap \mathcal{B}(\mathbf{x}_{\text{cp}}, r_{\text{cp}}) \neq \emptyset$ . Here,

$$\mathbf{x}_{\text{cp}} = \frac{1}{|P_{\text{cp}}|} \sum_{\mathbf{x}_i \in P_{\text{cp}}} \mathbf{x}_i,$$

$$P_{\text{cp}} := \{\mathbf{x} \in \tilde{\Sigma} : \min_{\mathbf{x}_i \in \Omega_c} \|\mathbf{x} - \mathbf{x}_i\|_2\}$$

and the radius  $r_{\text{cp}} = \max_{\mathbf{x} \in P_{\text{cp}}} \|\mathbf{x} - \mathbf{x}_{\text{cp}}\|_2$ .

Finally, after computing a tetrahedral decomposition of each interface cell, the volume fraction of a cell  $\Omega_c$  is calculated as

$$\alpha_c = \frac{1}{|\Omega_c|} \sum_{T \in T_c} \alpha(T) |\text{conv}(T)| \quad (27)$$

where  $T_c$  denotes the set of tetrahedra resulting from the decomposition of  $\Omega_c$  and  $|\text{conv}(T)|$  the volume of  $T$ . The volume fraction  $\alpha(T)$  is computed with the approach of Detrixhe and Aslam [10] (eq. 7), repeated here

$$\alpha(T) = \begin{cases} 1, & \phi_4 \leq 0, \\ 1 - \frac{\phi_4^3}{(\phi_4 - \phi_1)(\phi_4 - \phi_2)(\phi_4 - \phi_3)}, & \phi_3 \leq 0 < \phi_4, \\ 1 - \frac{\phi_1 \phi_2 (\phi_3^2 + \phi_3 \phi_4 + \phi_4^2) + \phi_3 \phi_4 (\phi_3 \phi_4 - (\phi_1 + \phi_2)(\phi_3 + \phi_4))}{(\phi_1 - \phi_3)(\phi_2 - \phi_3)(\phi_1 - \phi_4)(\phi_2 - \phi_4)}, & \phi_2 \leq 0 < \phi_3, \\ -\frac{\phi_1^3}{(\phi_2 - \phi_1)(\phi_3 - \phi_1)(\phi_4 - \phi_1)}, & \phi_1 \leq 0 < \phi_2, \\ 0 & \phi_1 > 0, \end{cases} \quad (28)$$

where  $\phi_4 \geq \phi_3 \geq \phi_2 \geq \phi_1$  are the signed distances at the vertices  $\mathbf{x}_i$  of  $T$ . The overall approach is summarized in algorithm 2.

---

**Algorithm 2** The Surface-Mesh / Cell Approximation Algorithm (SMCA)

---

- 1: Follow algorithm 1 up to step 13.
  - 2: Identify interface cells (eq. (23))
  - 3: Set bulk  $\alpha_c$  (eq. (24))
  - 4: Centroid decomposition of cells into tetrahedra (fig. 5)
  - 5: **for**  $l \in \{1, \dots, l_{\max}\}$  **do**
  - 6:     Flag tetrahedra for further refinement (eq. (23))
  - 7:     Decompose flagged tetrahedra (fig. 8)
  - 8:     Compute  $\phi$  for new points (eq. (14))
  - 9: **end for**
  - 10: Compute  $\alpha_c$  for interface cells (eq. (27))
- 

## 4. Results

The software implementation is available on GitLab [27]: we refer to the specific version (git tag) used to generate results described below. Detailed information on how to build and use the software is provided in the `README.md` file in the root folder of the software repository.

We use the difference between the total volume given by the volume fraction calculated from the surface on the unstructured mesh, and the exact volume bounded by the surface, namely

$$E_v = \frac{1}{V_e} \left| V_e - \sum_{c \in C} \alpha_c |\Omega_c| \right|, \quad (29)$$

as the measure of accuracy of the proposed algorithms. Here,  $V_e$  is the volume given by the exact surface function, or the volume that is bounded by a given surface mesh if an exact surface function is not available, e.g. in sections 4.2 and 4.3. In these cases, we calculate  $V_e$  using

$$V_e = \frac{1}{3} \left| \int_{V_e} \nabla \cdot \mathbf{x} dV \right| = \frac{1}{3} \left| \int_{\partial V_e} \mathbf{x} \cdot \mathbf{n} dS \right| \quad (30)$$

where  $\partial V_e$  is the surface that bounds  $V_e$ . As this surface is triangulated, eq. (30) can be expanded further

$$V_e = \frac{1}{3} \left| \sum_{t \in 1 \dots N_{\tilde{\Sigma}}} \int_{T_t} \mathbf{x} \cdot \mathbf{n} dS \right| = \frac{1}{3} \left| \sum_{t \in 1 \dots N_{\tilde{\Sigma}}} \int_{T_t} (\mathbf{x} - \mathbf{x}_t + \mathbf{x}_t) \cdot \mathbf{n} dS \right| = \frac{1}{3} \left| \sum_{t \in 1 \dots N_{\tilde{\Sigma}}} \mathbf{x}_t \cdot \mathbf{S}_t \right| \quad (31)$$

where  $N_{\tilde{\Sigma}}$  is the number of triangles in  $\tilde{\Sigma}$ ,  $T_t \in \tilde{\Sigma}$  are triangles that form the interface mesh, and  $\mathbf{x}_t, \mathbf{S}_t$  are their respective centroids and area normal vectors.

Computing architecture	
CPU	vendor_id : AuthenticAMD cpu family : 23 model : 49 model name : AMD Ryzen Threadripper 3990X 64-Core Processor frequency : 2.90 GHz
Compiler	version : g++ (Ubuntu 10.2.0-5ubuntu1 20.04) 10.2.0 optimization flags : -std=c++2a -O3

Table 1: Used computing architecture.

Table 1 contains the details on the computing architectures used to report the absolute CPU times in the result section. We have fixed the CPU frequency to 2.9GHz to stabilize the CPU time measurements.

#### 4.1. Sphere and ellipsoid

Exact initialization algorithms for spheres are available on unstructured meshes [46, 25]. We use the sphere and ellipsoid test cases to confirm the second-order convergence of SMCI/A algorithms and their applicability as a volume fraction model for the unstructured Level Set / Front Tracking method [28, 51]. The sphere case consists of a sphere with a radius  $R = 0.15$ , and the ellipsoid half-axes are (0.4, 0.3, 0.2). Both the sphere and ellipsoid center are at (0.5, 0.5, 0.5), in a unit box domain. Error convergence, CPU time and additional data are publicly available [31].

##### 4.1.1. SMCI Algorithm

Figure 9 shows the expected second-order convergence of the global error  $E_v$  given by eq. (29) on cubic fig. 9a and irregular hexahedral fig. 9b unstructured meshes. In fig. 9,  $N_c$  is the number of cells used along each spatial dimension of  $\tilde{\Omega}$  and  $N_T$  is the number of triangles used to resolve the sphere.

The CPU times reported in fig. 10 for the architecture A1 in table 1 show that the SMCI algorithm is a promising candidate for a volume fraction model for the unstructured Level Set

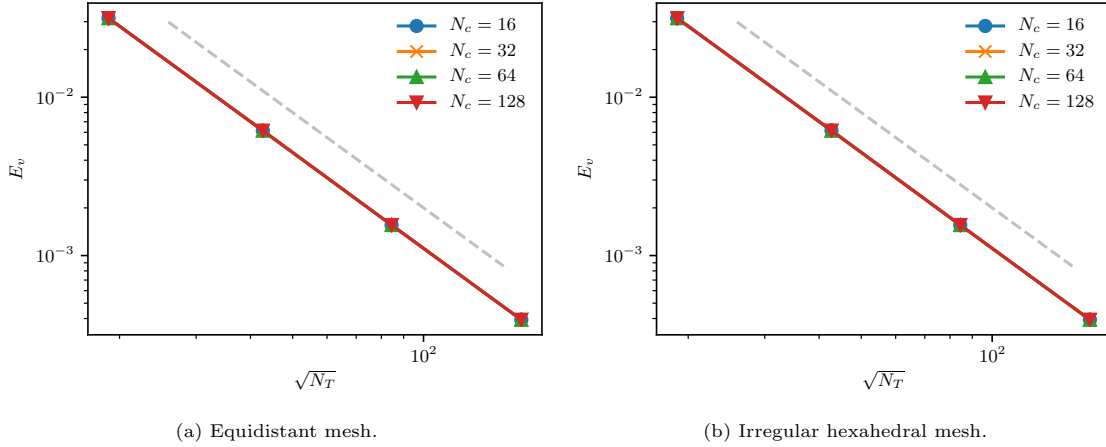


Figure 9:  $E_v$  errors of the SMCI algorithm for the sphere. The grey dashed line indicates second order convergence.

/ Front Tracking method. The complexity of the algorithm expressed in terms of the measured CPU time remains, linear for a constant ratio  $\sqrt{N_T}/N_c$ . The computational complexity increases to quadratic with an increasing number of triangles per cell  $\sqrt{N_T}/N_c$ : this happens when a very fine surface mesh is used to compute volume fractions on a very coarse volume mesh. An intersection between a highly resolved surface mesh and single cell of a relatively coarse mesh is shown in fig. 11a.

This configuration is relevant for accurate initialization of volume fractions on coarse meshes, but irrelevant for calculating the phase indicator for Front Tracking, where only a small number of triangles per multimaterial cell ( $\leq 10$ ) is present. Therefore, linear complexity of the SMCI algorithm for small ratios  $\sqrt{N_T}/N_c$  makes SMCI a potential candidate for a highly accurate geometrical volume fraction model for the unstructured Level Set / Front Tracking method. We will investigate this possibility in our future work. When considering the absolute CPU times, it is important to note that the SMCI algorithm has not yet been optimized for performance.

The volume error  $E_v$  for a sphere is shown in fig. 9b for a perturbed hexahedral mesh. An example perturbed mesh from this parameter study is shown in fig. 11b. The mesh is distorted by randomly perturbing cell corner points, using a length scale factor  $\alpha_e \in [0, 1]$  for the edges  $e$  that surround the mesh point. We have used  $\alpha_e = 0.25$ , resulting in perturbations that are of the size of  $0.25 \times$  the edge length. This results in a severe perturbation of the mesh shown in fig. 11b, as well as non-planarity of the faces of hexahedral cells. Still, as shown in fig. 9b, SMCI retains second-order convergence, which is also the case for the initialization of the ellipsoid on the equidistant fig. 12 and perturbed hexahedral mesh fig. 12b.

#### 4.1.2. SMCA algorithm

First, the effectiveness of the local adaptivity employed in the SMCA algorithm is examined with a spherical interface as described in section 4.1. Resolution of the volume mesh is fixed to  $N_c = 16$  cells in each direction while the sphere is resolved with  $\sqrt{N_T} \approx 410$  triangles. Maximum refinement levels  $l_{\max}$  from 0 to 3 are manually prescribed. In fig. 13, the resulting global volume errors  $E_v$  are displayed. This test case confirms the expected second-order convergence of  $E_v$  with adaptive refinement. An exemplary tetrahedral decomposition of a perturbed hex cell with a part of the the surface mesh is displayed in fig. 14. It demonstrates that the adaptive refinement based on the

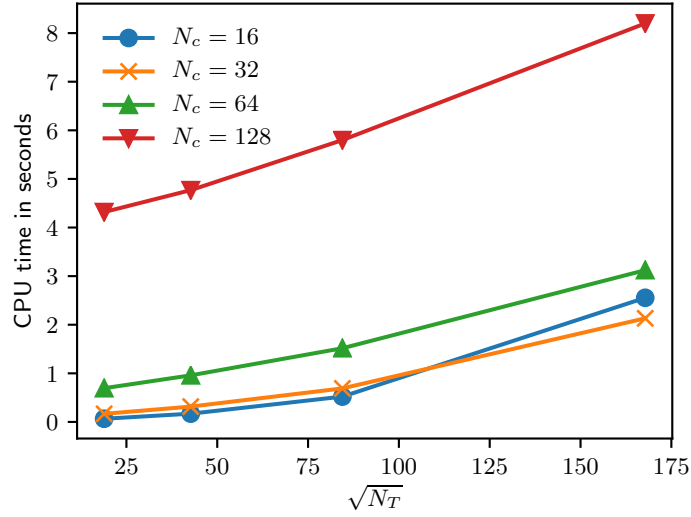
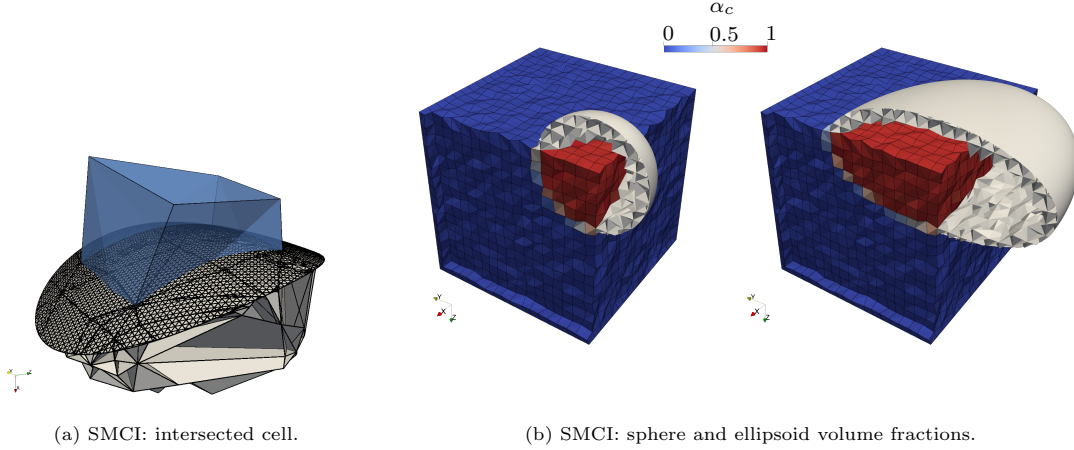


Figure 10: CPU times of the SMCI algorithm for the sphere initialized on a cubic unstructured mesh.



(a) SMCI: intersected cell.

(b) SMCI: sphere and ellipsoid volume fractions.

Figure 11: SMCI algorithm used with a sphere and an ellipsoid on an unstructured hexahedral mesh.

bounding ball criterion eq. (23) works as intended. Refinement is localized to the vicinity around the interface. Yet, the approach ensures all tetrahedra intersected by the interface are actually refined. The effectiveness of the local adaptive refinement compared to a uniform one becomes apparent when comparing the resulting number of tetrahedra. Our adaptive approach yields around 2247 tetrahedra per interface cell on average for the spherical interface with  $\sqrt{N_T} \approx 410$ ,  $N_c = 16$  and  $l_{\max} = 3$ . A uniform decomposition, on the contrary, would result in  $M_i \times M_r^{l_{\max}} = 24 \times 8^3 \approx 47.9 \times 10^3$  tetrahedra, where  $M_i$  denotes the number of tetrahedra from initial cell decomposition and  $M_r$  the number of tetrahedra from refining a tetrahedron. Thus, the local adaptive refinement reduces the

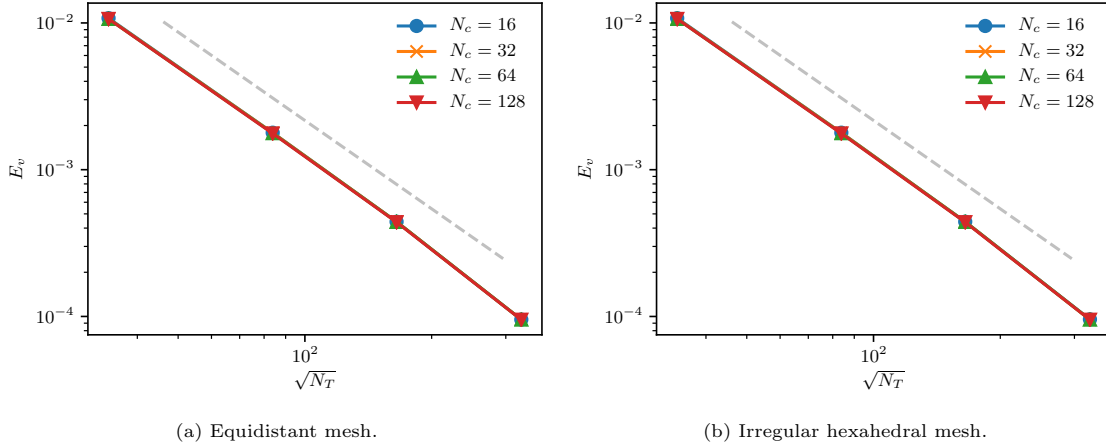


Figure 12:  $E_v$  errors of the SMCI algorithm for the ellipsoid. The grey dashed line indicates second order convergence.

required overall number of tetrahedra by a factor of 5.5 in comparison to a uniform refinement, without affecting the accuracy.

Having verified the refinement procedure, accuracy of the SMCA algorithm and its convergence with respect to surface mesh resolution is assessed in the following. As for the SMCI algorithm, a sphere and an ellipsoid are used for this purpose. Results for the sphere in terms of the global volume error  $E_v$  (eq. (29)) are shown in fig. 15 for cubic cells (fig. 15a) and perturbed hexahedral cells (fig. 15b). Domain size, sphere centre and radius are identical to the SMCI setup as well as the perturbation factor  $\alpha_e = 0.25$ . The maximum refinement level is computed according to eq. (26). Both mesh types yield nearly identical results and show second-order convergence. Resolution of the volume mesh  $N_c$  has a minor influence for coarser surface meshes which vanishes for  $\sqrt{N_T} > 100$ . For the ellipsoidal interface, the errors  $E_v$  are shown in fig. 16. The results are qualitatively and quantitatively similar to those of the spherical interface. Absolute computational times required for the initialization of a sphere with the SMCA algorithm are displayed in fig. 17. Run times have been measured on the architecture listed in table 1. As the implementation SMCI algorithm, our implementation of the SMCA algorithm has not yet been optimized for performance.

Because of the algebraic calculation of volume fractions from signed distances, the SMCA algorithm allows a direct comparison with volume fraction initialization methods on unstructured meshes that represent the fluid interface using function composition. Considering section 1, logical choices for the comparison are the methods of Ahn and Shashkov [1], Fries and Omerović [13], Jones et al. [21]. However, Ahn and Shashkov [1] do not provide convergence results for the 3D initialization and Fries and Omerović [13] integrate a function that is  $\neq 1$  within their 3D surface, so the result of the quadrature does not correspond to the volume enclosed by the surface. We therefore provide a direct comparison with Jones et al. [21], specifically Jones et al. [21, table 3].

Absolute volume errors are computed for an octant of a sphere with radius  $R = 0.5$ , placed at  $(0, 0, 0)$  within a unit-length cubical domain, and are shown in fig. 18. Tetrahedral unstructured meshes are generated using the Delaunay algorithm in `gmsh` [14], by providing a discretization length that results in a number of mesh points comparable to Jones et al. [21, table 3, No Nodes]. As shown in fig. 18, the accuracy of the SMCA algorithm depends on the volume mesh resolution

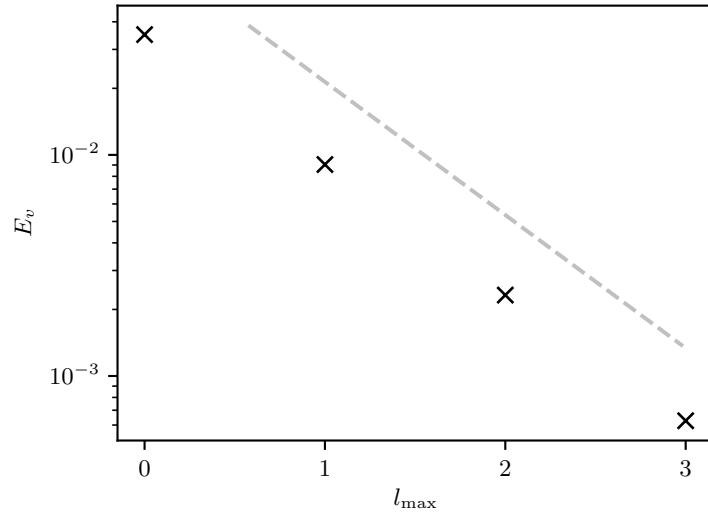


Figure 13:  $E_v$  errors of the SMCA algorithm using different refinement levels  $l_{\max}$  for a sphere. Resolution of volume and surface mesh are fixed to  $N_c = 16$  and  $\sqrt{N_T} \approx 410$ . The grey dashed line indicates second order convergence.

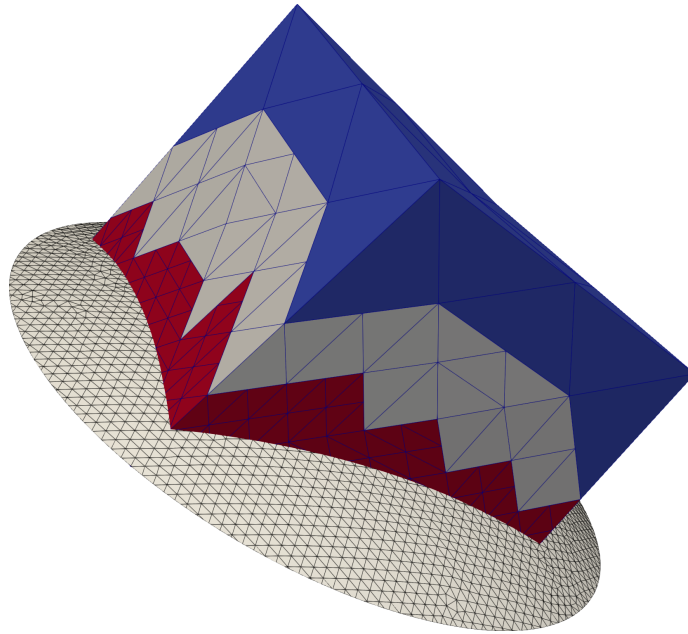


Figure 14: Tetrahedral decomposition of a perturbed hex cell used to approximate  $\alpha_c$ . Tetrahedra from different refinement levels are shown in different colors (level 1: blue, level 2: grey, level 3: red). Due to adaptivity, the highest refinement level is localized in the vicinity of the surface mesh..

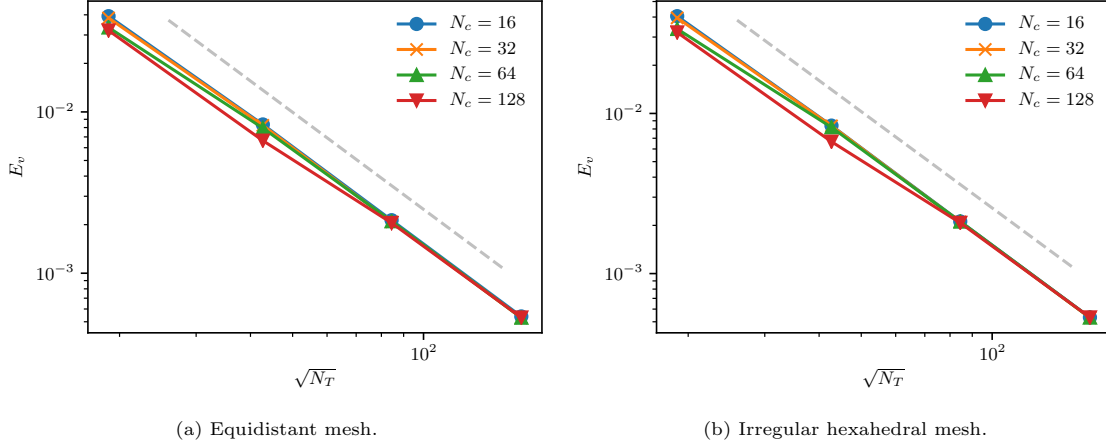


Figure 15:  $E_v$  errors of the SMCA algorithm for the sphere. The grey dashed line indicates second order convergence.

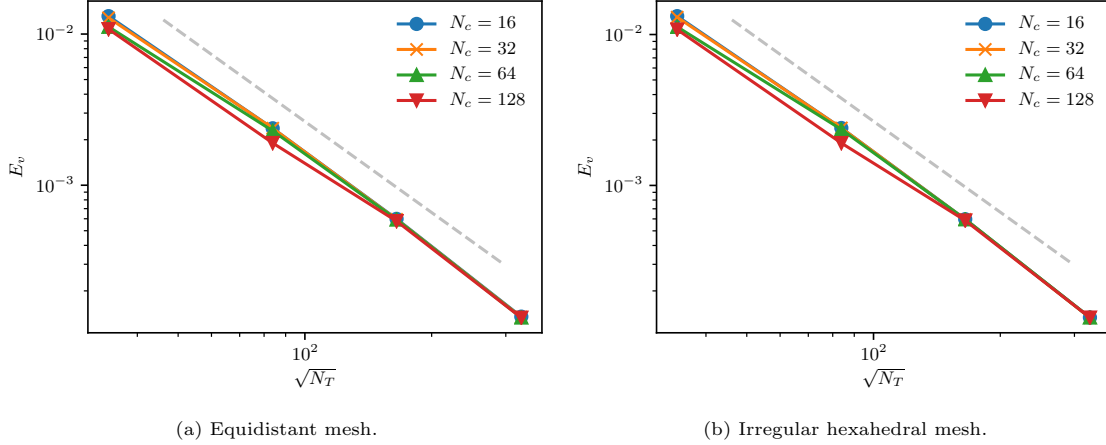


Figure 16:  $E_v$  errors of the SMCA algorithm for the ellipsoid. The grey dashed line indicates second order convergence.

and the number of refinement levels when an implicit (exact) sphere is used as interface description. This is expected since both parameters influence the size of the refined tetrahedra which are used to approximate the volume fraction. Consequently, the achievable accuracy is not limited by the volume mesh resolution and can be controlled through the number of refinement levels. The lowest absolute errors are in the order of magnitude of  $10^{-9}$ , achieved by SMCA using 10 refinement levels, and correspond to relative errors in the order of magnitude of  $10^{-8}$ , which is around 4 orders of magnitude lower than minimal VOF advection errors reported so far in the literature [30], and are therefore admissible as initial volume fraction values. Even higher levels of absolute accuracy, comparable to Jones et al. [21, table 3,  $\bar{\epsilon}_6, \bar{\epsilon}_9$ ], can be achieved with further refinement, with substantially increased computational expense. However, such further increase in accuracy is

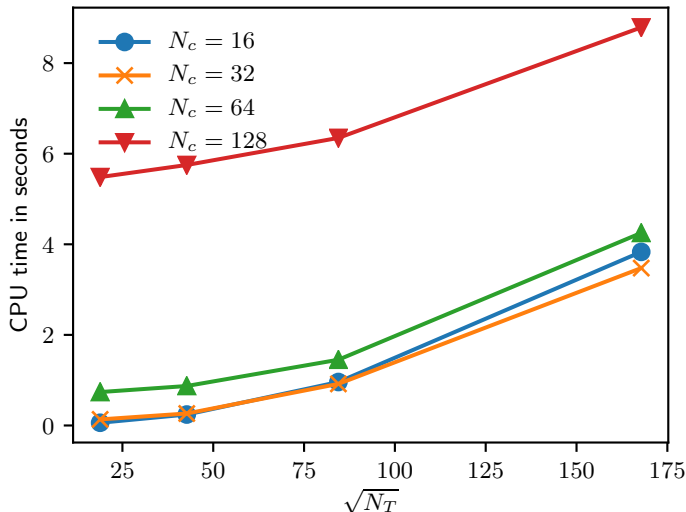


Figure 17: CPU times of the SMCA algorithm for the sphere initialized on a cubic unstructured mesh.

without significance to the volume fraction advection [30]. Contrary to the implicit (exact) sphere, resolving a sphere using a triangular mesh is more challenging, as the absolute accuracy depends on the resolution of the surface mesh. Results for spheres triangulated using the Frontal Algorithm in `gmsh` [14] are shown in fig. 18. Doubling the resolution of the surface mesh, as expected, doubles the accuracy of SMCA with triangulated surfaces as input. This approach of course does not make sense for a sphere, whose implicit (exact) function is easily defined. For geometrically complex surfaces shown below, it is important to have in mind that the resolution of the surface mesh together with the refinement level determine the absolute accuracy and computational costs.

#### 4.2. Surface of a fluid from an experiment

Some methods that are surveyed in section 1 can initialize volume fractions from exact implicit surfaces, such as a sphere or an ellipsoid, analyzed in section 4.1. One novelty of SMCI/A algorithms is their ability to compute volume fractions from arbitrary surfaces on arbitrary unstructured meshes. For example, volume fractions given by an experimental surface were calculated by the SMCI algorithm in Hartmann et al. [16] for studying breakup dynamics of a capillary bridge on a hydrophobic stripe between two hydrophilic stripes. In [16], the experimental setup involves a liquid bridge that is formed between two larger droplets across a hydrophobic stripe. The hydrophobic stripe drives the collapse of this liquid bridge, that is observed experimentally and in a simulation in [16]. The quantitative comparison of the simulation and the experiment from [16] is shown in fig. 19a. The experimental surface from Hartmann et al. [16], used to initialize volume fractions, is shown in fig. 19b. The SMCI algorithm computes the volume fractions of the experimental fluid interface from [16] with the volume error  $E_v = 7.789e - 06$ . As shown in section 4.1, the accuracy of the initialization depends on the quality of the surface mesh, not on the resolution of the volume mesh, that is chosen in this case to appropriately resolve the hydrodynamics in [16].

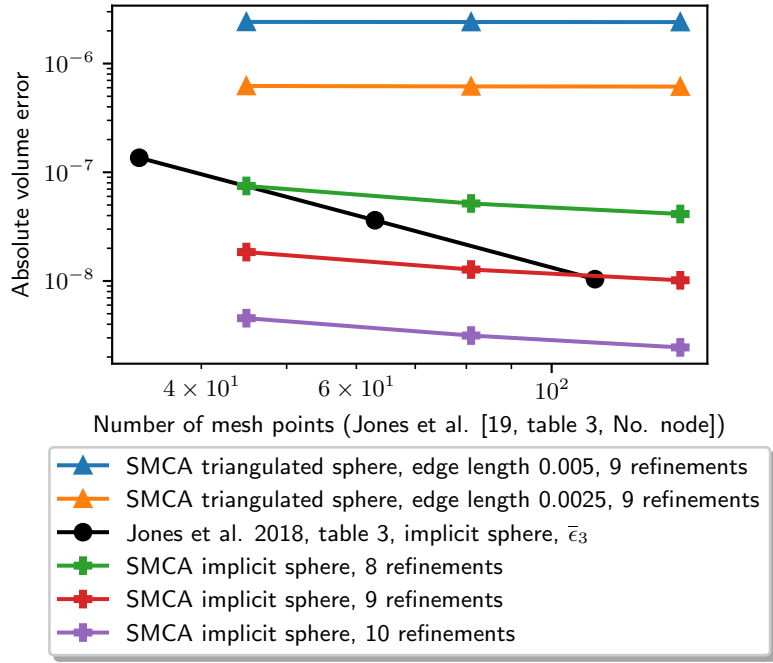
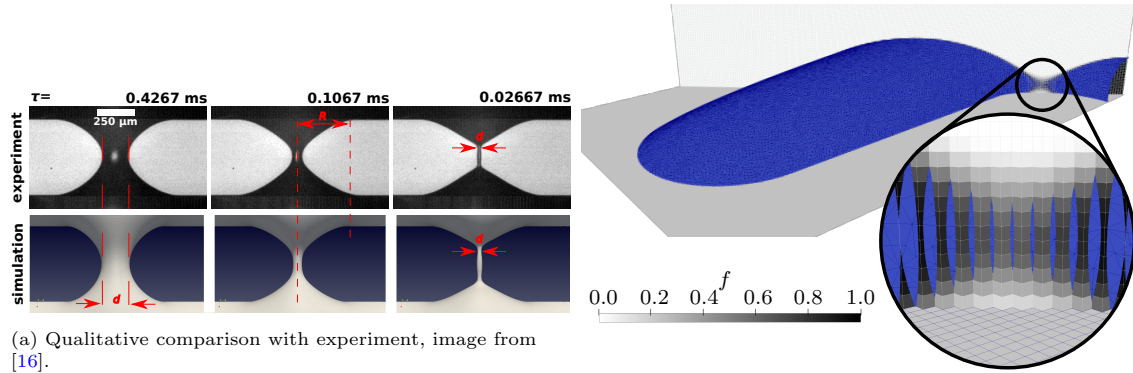


Figure 18: Comparing the SMCA algorithm and Jones et al. [21, table 3] on tetrahedral meshes.



(a) Qualitative comparison with experiment, image from [16].

(b) Initialization of volume fractions  $f$  for the wetting experiment, image adapted from [16].

Figure 19: Simulation of the wetting experiment with the fluid interface given as a triangular surface mesh [16].

### 4.3. CAD model

To demonstrate that the SMCI/A algorithms are able to handle interfaces more complex than shown in section 4.1 and section 4.2, the surface mesh from a CAD model displayed in fig. 20a is used. In contrast to the previous interfaces, this one features sharp edges and geometric features

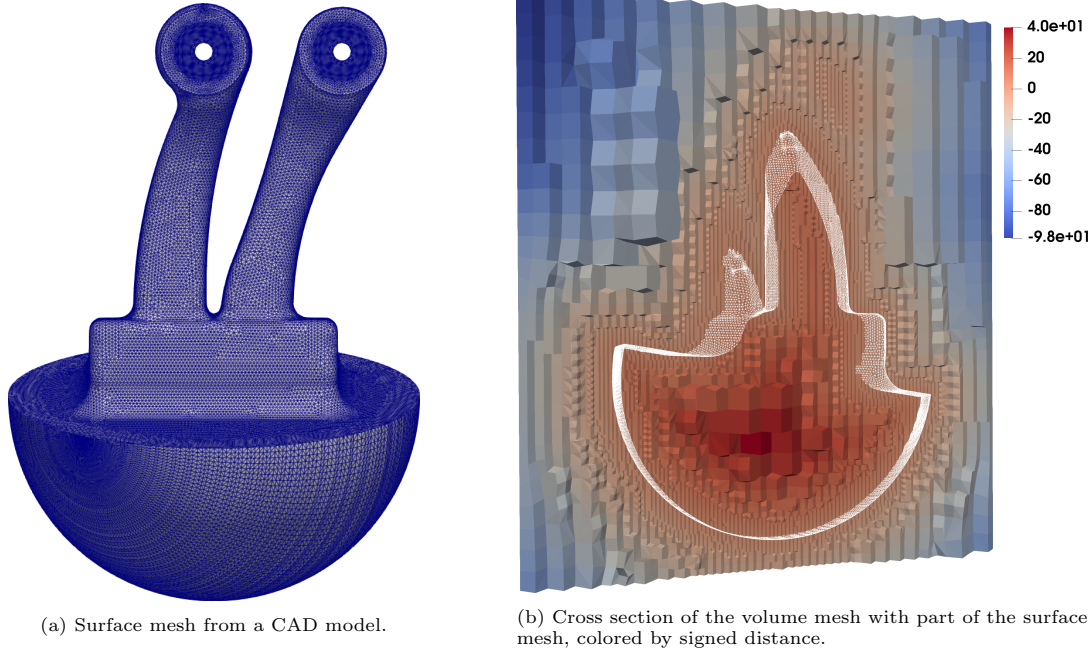


Figure 20: Surface and volume mesh of the CAD model test case.

of distinctly different sizes. The mesh for this test case has been generated with the *cartesianMesh* tool of cfMesh [22]. Refinement is used in the vicinity of the interface. This meshing procedure is chosen to obtain a mesh that closer resembles that of an industrial application than a uniform cubic mesh. A cross section of the mesh is depicted in fig. 20b. Before examining the computed volume fractions for this case, the signed distance calculation (section 2.2) and sign propagation (section 2.3) are verified. The presence of sharp edges (see fig. 20a) makes this test case more prone to false inside/outside classifications than the others shown so far. Yet our procedure yields the correct sign for the distance in all cells as shown in fig. 21a. The enclosed volume of the surface mesh is considered as  $\Omega^+$ , thus  $\phi > 0$  for all points  $\mathbf{x} \in \Omega^+$ . As displayed in fig. 21a and confirmed by further manual inspection of the results, the proposed signed distance calculation correctly classifies all cells within the narrow band and robustly propagates this information to the entire domain. This is reflected in the volume fractions as computed, shown in fig. 21b. Bulk cells are assigned values of either 1 or 0, depending on whether they are located in  $\Omega^+$  or  $\Omega^-$  and mixed cells with  $0 < \alpha_c < 1$  are only found where the surface mesh is located. Accuracy-wise, the global errors  $E_v$  depicted in fig. 22 have been obtained with the SMCA algorithm using different refinement levels. As for the spherical interface (see fig. 13), second-order convergence is achieved, even though the surface mesh approximates a non-smooth interface here.

## 5. Conclusions

The proposed Surface-Mesh Cell Intersection / Approximation algorithms accurately compute signed distances from arbitrary surfaces intersecting arbitrary unstructured meshes. Geometrical

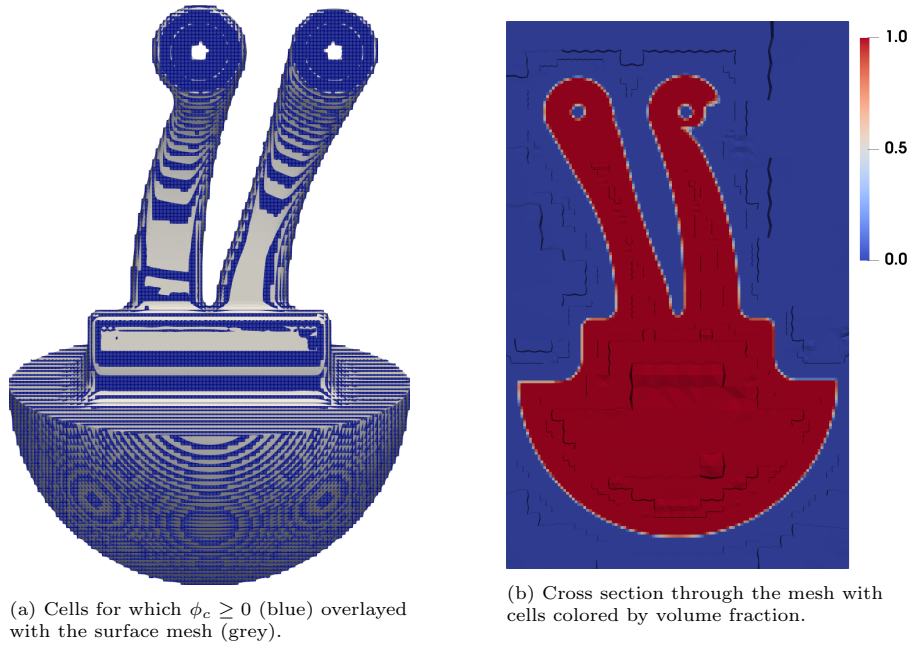


Figure 21: Inside/outside computation and resulting volume fractions for the CAD geometry.

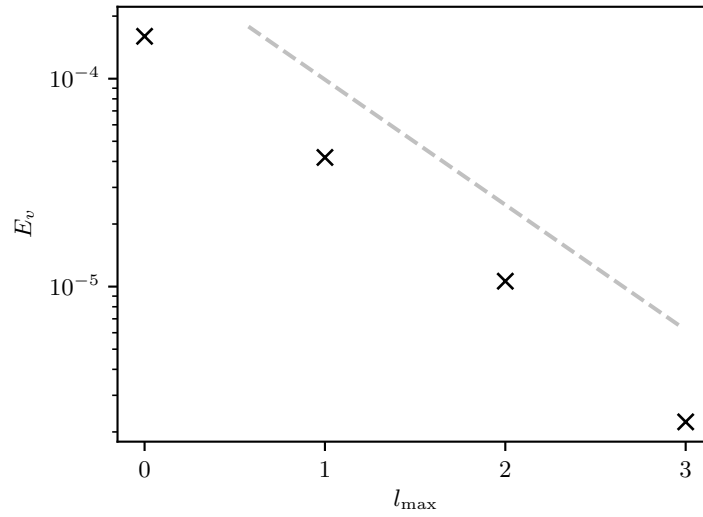


Figure 22:  $E_v$  errors of the SMCA algorithm using different refinement levels  $l_{\max}$  for the CAD model with the reference volume  $V_e$  computed by eq. (31). The grey dashed line indicates second order convergence.

calculations ensure the accuracy of signed distances near the discrete surface. The signed distances (actually their inside / outside information) are propagated into the bulk using the approximate

solution of a Laplace equation. Once the signed distances are available in the full simulation domain, the SMCI algorithm computes volume fractions by intersecting arbitrarily-shaped mesh cells with the given surface mesh, while the SMCA algorithm approximates volume fractions using signed distances stored at cell corner points. Both algorithms are robust and show second-order convergence for exact surfaces and arbitrarily shaped surface meshes. The SMCI algorithm scales linearly with a small number of surface triangles per cut-cell. Since a small number of triangles per cell is a requirement for Front Tracking, this linear-complexity makes SMCI an interesting candidate for computing volume fractions in the 3D unstructured Level Set / Front Tracking method [28, 51], which will be the subject of future investigations.

## 6. Acknowledgments

Calculations for this research were conducted on the Lichtenberg high performance computer of the TU Darmstadt.

Funded by the German Research Foundation (DFG) – Project-ID 265191195 – SFB 1194, Projects B02, B01 and Z-INF.

We are grateful for the discussions on the phase-indicator calculation in the LCRM method on structured meshes [45] with Prof. Dr. Seungwon Shin, Dr. Damir Juric, and Dr. Jalel Chergui within the project "Initiation of International Cooperations" MA 8465/1-1.

## References

- [1] H. T. Ahn and M. Shashkov. Multi-material interface reconstruction on generalized polyhedral meshes. Technical Report LA-UR-07-0656, 2007.
- [2] E. Aulisa, S. Manservigi, and R. Scardovelli. A mixed markers and volume-of-fluid method for the reconstruction and advection of interfaces in two-phase and free-boundary flows. *J. Comput. Phys.*, 188(2):611–639, 2003. ISSN 00219991. doi: 10.1016/S0021-9991(03)00196-7. URL [https://doi.org/10.1016/S0021-9991\(03\)00196-7](https://doi.org/10.1016/S0021-9991(03)00196-7).
- [3] E. Aulisa, S. Manservigi, R. Scardovelli, and S. Zaleski. Interface reconstruction with least-squares fit and split advection in three-dimensional Cartesian geometry. *J. Comput. Phys.*, 225(2):2301–2319, 2007. ISSN 00219991. doi: 10.1016/j.jcp.2007.03.015. URL <https://dx.doi.org/10.1016/j.jcp.2007.03.015>.
- [4] J. A. Baerentzen and H. Aanaes. Signed distance computation using the angle weighted pseudonormal. *IEEE Transactions on Visualization and Computer Graphics*, 11(3):243–253, 2005. doi: 10.1109/TVCG.2005.49. URL <https://doi.org/10.1109/TVCG.2005.49>.
- [5] S. Bnà, S. Manservigi, R. Scardovelli, P. Yecko, and S. Zaleski. Numerical integration of implicit functions for the initialization of the VOF function. *Comput. Fluids*, 113: 42–52, 2015. doi: 10.1016/j.compfluid.2014.04.010. URL <http://dx.doi.org/10.1016/j.compfluid.2014.04.010>.
- [6] S. Bnà, S. Manservigi, R. Scardovelli, P. Yecko, and S. Zaleski. Vofi - A library to initialize the volume fraction scalar field. *Comput. Phys. Commun.*, 200:291–299, 2016. ISSN 00104655. doi: 10.1016/j.cpc.2015.10.026. URL <http://dx.doi.org/10.1016/j.cpc.2015.10.026>.

- [7] S. J. Cummins, M. M. Francois, and Douglas B. Kothe. Estimating curvature from volume fractions. *Comput. Struct.*, 83(6-7):425–434, 2005. ISSN 00457949. doi: 10.1016/j.compstruc.2004.08.017. URL <http://dx.doi.org/10.1016/j.compstruc.2004.08.017>.
- [8] R. B. DeBar. Fundamentals of the KRAKEN code. *Tech. Rep.*, pages UCID–17366, 1974.
- [9] S. S. Desphande, L. Anumolu, and M. F. Trujillo. Evaluating the performance of the two-phase flow solver interFoam. *Comput. Sci. Discov.*, 5(014016):1—36, 2012. doi: 10.1088/1749-4699/5/1/014016. URL <https://doi.org/10.1088/1749-4699/5/1/014016>.
- [10] M. Detrixhe and T. D. Aslam. From level set to volume of fluid and back again at second-order accuracy. *Int. J. Numer. Methods Fluids*, 80:231–255, 2016. doi: 10.1002/fld. URL <https://dx.doi.org/10.1002/fld>.
- [11] Sai C Divi, Clemens V Verhoosel, Ferdinando Auricchio, Alessandro Reali, and E Harald Van Brummelen. Error-estimate-based adaptive integration for immersed isogeometric analysis. *Comput. Math. with Appl.*, 80(11):2481–2516, 2020. ISSN 0898-1221. doi: 10.1016/j.camwa.2020.03.026. URL <https://doi.org/10.1016/j.camwa.2020.03.026>.
- [12] M. M. Francois, S. J. Cummins, E. D. Dendy, D. B. Kothe, J. M. Sicilian, and M. W. Williams. A balanced-force algorithm for continuous and sharp interfacial surface tension models within a volume tracking framework. *J. Comput. Phys.*, 213(1):141–173, 2006. ISSN 00219991. doi: 10.1016/j.jcp.2005.08.004. URL <http://dx.doi.org/10.1016/j.jcp.2005.08.004>.
- [13] T. P. Fries and S. Omerović. Higher-order accurate integration of implicit geometries. *Int. J. Numer. Methods Eng.*, 106(5):323–371, 2016. ISSN 10970207. doi: 10.1002/nme.5121. URL <https://dx.doi.org/10.1002/nme.5121>.
- [14] Christophe Geuzaine and Jean-François Remacle. Gmsh: A 3-d finite element mesh generator with built-in pre-and post-processing facilities. *International journal for numerical methods in engineering*, 79(11):1309–1331, 2009.
- [15] S. Ghali. *Introduction to geometric computing*. Springer Science & Business Media, 2008. URL <https://www.springer.com/gp/book/9781848001145>.
- [16] Maximilian Hartmann, Mathis Fricke, Lukas Weimar, Dirk Gründing, Tomislav Marić, Dieter Bothe, and Steffen Hardt. Breakup dynamics of capillary bridges on hydrophobic stripes. *International Journal of Multiphase Flow*, page 103582, 2021.
- [17] C. W. Hirt and B. D. Nichols. Volume of fluid/VOF/ method for the dynamics of free boundaries. *J. Comput. Phys.*, 39(1):201–225, 1981. ISSN 00219991. doi: 10.1016/0021-9991(81)90145-5. URL [https://dx.doi.org/10.1016/0021-9991\(81\)90145-5](https://dx.doi.org/10.1016/0021-9991(81)90145-5).
- [18] C. B. Ivey and P. Moin. Accurate interface normal and curvature estimates on three-dimensional unstructured non-convex polyhedral meshes. *J. Comput. Phys.*, 300:365–386, 2015. ISSN 10902716. doi: 10.1016/j.jcp.2015.07.055. URL <http://dx.doi.org/10.1016/j.jcp.2015.07.055>.
- [19] H. Jasak. *Error analysis and estimation for the finite volume method with applications to fluid flows*. PhD thesis, 1996.

- [20] L. Jofre, O. Lehmkuhl, J. Castro, and A. Oliva. A 3-D Volume-of-Fluid advection method based on cell-vertex velocities for unstructured meshes. *Comput. Fluids*, 94:14–29, 2014. ISSN 00457930. doi: 10.1016/j.compfluid.2014.02.001. URL <http://dx.doi.org/10.1016/j.compfluid.2014.02.001>.
- [21] B. W.S. Jones, A. G. Malan, and N. A. Ilangakoon. The initialisation of volume fractions for unstructured grids using implicit surface definitions. *Comput. Fluids*, 179:194–205, 2019. ISSN 00457930. doi: 10.1016/j.compfluid.2018.10.021. URL <https://doi.org/10.1016/j.compfluid.2018.10.021>.
- [22] F. Juretić. The cfMesh library for polyhedral mesh generation. <https://sourceforge.net/projects/cfmesh/>. Accessed: 2020-01-15.
- [23] F. Juretić. *Error analysis in finite volume CFD*. PhD thesis, Imperial College London (University of London), 2005.
- [24] Hyun-Jung Kim, Yu-Deok Seo, and Sung-Kie Youn. Isogeometric analysis for trimmed CAD surfaces. *Comput. Methods Appl. Mech. Eng.*, 198(37-40):2982–2995, 2009.
- [25] J. Kromer and D. Bothe. Highly accurate computation of volume fractions using differential geometry. *J. Comput. Phys.*, 396(July):761–784, 2019. ISSN 00219991. doi: 10.1016/j.jcp.2019.07.005. URL <https://dx.doi.org/10.1016/j.jcp.2019.07.005>.
- [26] J. López, J. Hernández, P. Gómez, and F. Faura. Non-convex analytical and geometrical tools for volume truncation, initialization and conservation enforcement in VOF methods. *J. Comput. Phys.*, 392:666–693, 2019. ISSN 10902716. doi: 10.1016/j.jcp.2019.04.055. URL <https://doi.org/10.1016/j.jcp.2019.04.055>.
- [27] T. Marić, T. Tolle, and D. Gründing. The argo OpenFOAM module: the implementation of Surface Mesh Cell Intersection / Approximation algorithms. <https://gitlab.com/leia-methods/argo/-/tree/2021-10-27-SMCIA-R1>. Accessed: 2021-02-16.
- [28] T. Marić, H. Marschall, and D. Bothe. lentFoam – A hybrid Level Set/Front Tracking method on unstructured meshes. *Comput. Fluids*, 113:20–31, may 2015. ISSN 00457930. doi: 10.1016/j.compfluid.2014.12.019. URL <https://dx.doi.org/10.1016/j.compfluid.2014.12.019>.
- [29] T. Marić, H. Marschall, and D. Bothe. An enhanced un-split face-vertex flux-based VoF method. *J. Comput. Phys.*, 371:967–993, apr 2018. ISSN 10902716. doi: 10.1016/j.jcp.2018.03.048. URL <https://doi.org/10.1016/j.jcp.2018.03.048>.
- [30] T. Marić, D. B. Kothe, and D. Bothe. Unstructured un-split geometrical volume-of-fluid methods—a review. *Journal of Computational Physics*, 420:109695, 2020. doi: 10.1016/j.jcp.2020.109695. URL <https://doi.org/10.1016/j.jcp.2020.109695>.
- [31] Tomislav Maric, Tobias Tolle, and Dirk Gruending. Computing volume fractions and signed distances from arbitrary surfaces on unstructured meshes, October 2021. URL <https://doi.org/10.5281/zenodo.5603255>.
- [32] D. Meagher. Geometric modeling using octree encoding. *Comput. Graph. Image Process.*, 19(2):129–147, 1982. ISSN 0146664X. doi: 10.1016/0146-664X(82)90104-6. URL [http://dx.doi.org/10.1016/0146-664X\(82\)90104-6](http://dx.doi.org/10.1016/0146-664X(82)90104-6).

- [33] D. P. Mehta and S. Sahni. *Handbook of data structures and applications*. CRC Press, 2004.
- [34] S. Menon and D. P. Schmidt. Conservative interpolation on unstructured polyhedral meshes: An extension of the supermesh approach to cell-centered finite-volume variables. *Comput. Methods Appl. Mech. Eng.*, 200(41-44):2797–2804, 2011. ISSN 00457825. doi: 10.1016/j.cma.2011.04.025. URL <http://dx.doi.org/10.1016/j.cma.2011.04.025>.
- [35] F. Moukalled, L. Mangani, and M. Darwish. *The finite volume method in computational fluid dynamics*, volume 113. Springer, 2016. URL <https://www.springer.com/de/book/9783319168739>.
- [36] Alessandro Nitti, Josef Kiendl, Alessandro Reali, and Marco D de Tullio. An immersed-boundary/isogeometric method for fluid–structure interaction involving thin shells. *Computer Methods in Applied Mechanics and Engineering*, 364:112977, 2020.
- [37] W. F. Noh and P. R. Woodward. SLIC (Simple Line Interface Calculation) method. *Proc. Fifth Int. Conf. Numer. Methods Fluid Dyn. June 28–July 2, 1976 Twente Univ. Enschede*, pages 330–340, 1976. doi: 10.1007/3-540-08004-X\_336. URL [https://dx.doi.org/10.1007/3-540-08004-X\\_336](https://dx.doi.org/10.1007/3-540-08004-X_336).
- [38] M. Owkes and O. Desjardins. A mesh-decoupled height function method for computing interface curvature. *J. Comput. Phys.*, 281:285–300, 2015. ISSN 10902716. doi: 10.1016/j.jcp.2014.10.036. URL <https://dx.doi.org/10.1016/j.jcp.2014.10.036>.
- [39] M. Owkes and O. Desjardins. A mass and momentum conserving unsplit semi-Lagrangian framework for simulating multiphase flows. *J. Comput. Phys.*, 332:21–46, 2017. ISSN 10902716. URL <http://dx.doi.org/10.1016/j.jcp.2016.11.046>.
- [40] W. J. Rider and D. B. Kothe. Reconstructing Volume Tracking. *J. Comput. Phys.*, 141(2): 112–152, 1998. ISSN 00219991. doi: 10.1006/jcph.1998.5906. URL <https://doi.org/10.1006/jcph.1998.5906>.
- [41] G. Russo and P. Smereka. A Remark on Computing Distance Functions. *J. Comput. Phys.*, 163(1):51–67, 2000. ISSN 00219991. doi: 10.1006/jcph.2000.6553. URL <https://dx.doi.org/10.1006/jcph.2000.6553>.
- [42] H. Scheufler and J. Roenby. Accurate and efficient surface reconstruction from volume fraction data on general meshes. *J. Comput. Phys.*, 383:1–23, apr 2019. ISSN 10902716. doi: 10.1016/j.jcp.2019.01.009. URL <https://doi.org/10.1016/j.jcp.2019.01.009>.
- [43] Robert Schmidt, Roland Wüchner, and Kai-Uwe Bletzinger. Isogeometric analysis of trimmed NURBS geometries. *Comput. Methods Appl. Mech. Eng.*, 241:93–111, 2012.
- [44] S. Shin and D. Juric. Modeling Three-Dimensional Multiphase Flow Using a Level Contour Reconstruction Method for Front Tracking without Connectivity. *J. Comput. Phys.*, 180(2): 427–470, 2002. ISSN 00219991. doi: 10.1006/jcph.2002.7086. URL <https://dx.doi.org/10.1006/jcph.2002.7086>.
- [45] S. Shin, I. Yoon, and D. Juric. The Local Front Reconstruction Method for direct simulation of two- and three-dimensional multiphase flows. *J. Comput. Phys.*, 230(17):6605–6646, 2011. ISSN 00219991. doi: 10.1016/j.jcp.2011.04.040. URL <http://dx.doi.org/10.1016/j.jcp.2011.04.040>.

- [46] S. Strobl, A. Formella, and T. Pöschel. Exact calculation of the overlap volume of spheres and mesh elements. *J. Comput. Phys.*, 311:158–172, 2016. ISSN 10902716. doi: 10.1016/j.jcp.2016.02.003. URL <http://dx.doi.org/10.1016/j.jcp.2016.02.003>.
- [47] M. Sussman and E. Fatemi. An efficient, interface-preserving level set redistancing algorithm and its application to interfacial incompressible fluid flow. *SIAM Journal on scientific computing*, 20(4):1165–1191, 1999. doi: 10.1137/S1064827596298245. URL <https://doi.org/10.1137/S1064827596298245>.
- [48] M. Sussman, E. Fatemi, P. Smereka, and S. Osher. An improved level set method for incompressible two-phase flows. *Computers & Fluids*, 27(5-6):663–680, 1998. doi: 10.1016/S0045-7930(97)00053-4. URL [https://doi.org/10.1016/S0045-7930\(97\)00053-4](https://doi.org/10.1016/S0045-7930(97)00053-4).
- [49] M. Sussman, A. S. Almgren, J. B. Bell, P. Colella, L. H. Howell, and M. L. Welcome. An adaptive level set approach for incompressible two-phase flows. *Journal of Computational Physics*, 148(1):81–124, 1999. doi: 10.1006/jcph.1998.6106. URL <https://doi.org/10.1006/jcph.1998.6106>.
- [50] G. Thürrner and Wüthrich C. A. Computing vertex normals from polygonal facets. *Journal of Graphics Tools*, 3(1):43–46, 1998. doi: 10.1080/10867651.1998.10487487. URL <https://doi.org/10.1080/10867651.1998.10487487>.
- [51] T. Tolle, D. Bothe, and T. Marić. SAAMPLE: A Segregated Accuracy-driven Algorithm for Multiphase Pressure-Linked Equations. *Comput. Fluids*, 200:104450, 2020. ISSN 00457930. doi: 10.1016/j.compfluid.2020.104450. URL <https://dx.doi.org/10.1016/j.compfluid.2020.104450>.
- [52] C. D. Toth, J. O’Rourke, and Jacob E. Goodman. *Handbook of discrete and computational geometry*. Chapman and Hall/CRC, 2017.
- [53] G. Tryggvason, B. Bunner, A. Esmaeeli, D. Juric, N. Al-Rawahi, W. Tauber, J. Han, S. Nas, and Y. J. Jan. A front-tracking method for the computations of multiphase flow. *J. Comput. Phys.*, 169(2):708–759, 2001. ISSN 00219991. doi: 10.1006/jcph.2001.6726. URL <https://doi.org/10.1006/jcph.2001.6726>.
- [54] O. Ubbink. *Numerical prediction of two fluid systems with sharp interfaces*. PhD thesis, Imperial College of Science, Technology and Medicine, 1997.